12-2009

MECHANICAL AND CHEMICAL CHARACTERIZATION OF BIOLOGICAL COMPOSITE STRUCTURES

Bonnie Zimmerman
Clemson University, bonnie.leigh.zimmerman@gmail.com

MECHANICAL AND CHEMICAL CHARACTERIZATION OF BIOLOGICAL COMPOSITE STRUCTURES

A Thesis
Presented to
the Graduate School of
Clemson University

In Partial Fulfillment
of the Requirements for the Degree
Masters of Science
Materials Science and Engineering

By
Bonnie Leigh Zimmerman
December 2009

Accepted by:
M. Kennedy, Committee Chair
D. Dean
M. Ellison
I. Luzinov

ABSTRACT

A better understanding of the bioresponse of naturally occurring systems will help to optimize the engineering of synthetic biomaterials. The aim of this thesis was to characterize the mechanical and chemical behavior of two distinct biological composite systems, human teeth and wool fibers. These mechanical and chemical properties were also studied as a function of natural structure and environmental conditions.

Human teeth are composite systems consisting primarily of hydroxylapatite and protein. This project investigated how the use of clinical dental treatments and procedures, such as whitening and etching, affects mechanical properties. Analysis of nanoindentation with the Oliver-Pharr model provided elastic modulus and hardness across the DEJ. Mechanical properties of autoclaved and non-autoclaved teeth were measured to ensure both comparability to published values and relevance to clinical applications. Large increases were observed in the elastic modulus of enamel with autoclaving (52.0GPa versus 113.4GPa), while smaller increases were observed in the dentin (17.9GPa versus 27.9GPa). There was a similar trend in the increase in hardness of enamel (2.0GPa versus 4.3GPa) and dentin (0.5GPa versus 0.7GPa) when subjected to autoclaving. This work shows that the range of values previously reported in literature may be due largely to the sterilization procedures. Treatment of the exterior of non-autoclaved teeth with Crest Whitestrips™, Opalescence™ or UltraEtch™ caused changes in the mechanical properties of both the enamel and dentin. Those treated with Crest Whitestrips™ showed a reduction in the elastic modulus of enamel (55.3GPa to 32.7GPa)

and increase in the elastic modulus of dentin (17.2GPa to 24.3GPa). Opalescence™ treatments did not show a significant affect on the enamel properties, but did result in a decrease in modulus of dentin (18.5GPa to 15.1GPa). Additionally, UltraEtch™ treatment decreased the modulus and hardness of enamel (48.7GPa to 38.0GPa and 1.9GPa to 1.5GPa, respectively) and dentin (21.4GPa to 15.0GPa and 1.9GPa to 1.5GPa, respectively). These changes were linked to the change in protein content, verified by FTIR and fluorescence microscopy.

The second study characterized the amino acid distribution on the surface of Merino wool fibers. Although previous research identified which amino acids compose wool fibers, this was the first study to determine the amino acids distribution along the surface. Specifically, which amino acids have high concentrations near topographical surface features, such as the scale ridges. The distribution and types of amino acids along the surface of wool fibers was analyzed using force spectroscopy techniques. Initial measurements in phosphate buffer solution (PBS) showed carboxyl acid groups, aspartic acids and glutamic acids, are randomly distributed over the surface of wool fibers. Clusters of sulfur groups, cysteines, are uniformly distributed. In addition, the amine groups, arginine and lysine, are concentrated near the edge of scales. SEM images of wool fibers coated with functionalized nanoparticles were used to verify these results. The SEM images showed the binding sites of various charged chemical groups. To distinguish between positively charged surface groups, force spectroscopy was done under elevated pH, indicating a high contribution of lysine just below the edge of the scale.

DEDICATION

For everyone who has touched my life

and helped me to keep learning along the way.

ACKNOWLEDGMENTS

Thanks to God above all. He fixed breath unto my soul, grace unto my life, and meaning to every day. God grants me the direction, courage, and patience in the course of my study.

To Trevor, my amazing husband, the love of my life, who held my hand and believed in me, my heartfelt thanks.

I would like to thank my mom, dad and my little brother, Jake. During my studies toward the completion of my Masters degree, their encouragement has been immensely strengthening.

My gratitude also goes to Dr. M. Kennedy, who gave me a challenge and taught me the way. Thanks for guidance, patience, and support. I'm very appreciative of my advising committee members Dr. D. Dean, Dr. M. Ellison, and Dr. I. Luzinov for dedicating their valuable time to serve on my committee and offering continuous advisement throughout. Thanks to my group members, Isaac Rook, Julie Reid, Nathan Mitchell, and Jackie Wilkinson who listened to my research progress. Thank you to Dr. J. Harriss, who welcomed me into the photolithography lab and offered equipment, training, and valuable insight. In addition, I would like to thank Ms. Ivey for FTIR characterization, Ms. Jenkins for consultation on teeth preparation and stabilization, Laura Datko for collaboration on the mechanical characterization of teeth, and James Chow for involvement in nanoparticle functionalization on wool. Thanks to Dr. Satish Alapati at the Medical University of South Carolina for providing the teeth in this study.

Financial support was provided by the National Science Foundation's Division of Materials Research REU program under grant number 0453554, Kentwool and the School of Material Science and Engineering.

TABLE OF CONTENTS

Page

TABLE OF CONTENTS (Continued)

Page

TABLE OF CONTENTS (Continued)

Page #

LIST OF FIGURES

Chapter 2

Chapter 3

List of Figures (Continued)

Figure Page

Chapter 4

Figure Page

List of Figures (Continued)

Figure Page

LIST OF TABLES

CHAPTER ONE

INTRODUCTION

Characterization of the bioresponse of naturally occurring systems may further optimize the engineering of biomedical devices. This bioresponse, a living organism's reaction to external stimulus, may lead to control cell response, allow for the design of improved biomimetic materials, or permit the development of predictive models of biomaterial behavior. The research outlined here aims to characterize the mechanical and chemical response of two distinct biological composite systems, human teeth and wool fibers, in their natural state and after exposure to various environmental conditions.

1.1 Background

A biomaterial can be defined as part of a living structure or biomedical device [1.1]. The composite nature of many biomaterials allows for the achievement of distinct physical and chemical characteristics. Composite materials are combinations of two or more materials differing in form or composition [1.2] (*e.g.,* reinforcing elements, fillers, and composite matrix binders). Environmental conditions often contribute to the chemical and mechanical behavior of a biological composite. Characterization of mechanical behavior and surface chemistry draw the attention of global research efforts in medicine, dentistry, biology, chemistry, bioengineering and materials science because of the profound impacts on the development of biomaterials.

Mechanical and chemical properties of a substrate may influence the behavior of the external environment. Rather than merely supplying an inert scaffold or temporary framework, biomaterials are approaching the capability of effectively manipulating

biological responses [1.3-8]. Previous research has indicated that both chemical and physical surface properties control cellular response [1.9-10], thus the potential of biomedical devices has been progressing from “biocompatible” towards “bioactive”. Bioresponse is influenced by mechanical properties (*e.g.,* hardness and elastic modulus) as well as surface chemistry (*e.g.,* charges, homogeneity, hydrophobicity/ hydrophilicity, surface energy, and the presence specific functional groups). Bioresponse includes altered cell or peptide behavior, i.e., migration, adhesion [1.11], proliferation, growth and/or function [1.12, 1.13-14]. Viesha *et al.* demonstrated protein-patterning based on surface chemistry [1.15], while Zreigat *et al.* suggested that bone tissue integration is altered in the incorporation of ions onto a substrate [1.16][1.17]. Alternatively, Craighead *et al.* outlined the nerve cell response to substrates of various mechanical properties [1.18]. The control of cell behavior could present a wide-range of applications [1.6-8], further optimizing synthetic material cooperation with biological materials [1.18], allowing for more controlled drug delivery and enhanced coatings for medical devices [1.19].

Additionally, investigations of the mechanical and chemical properties of naturally occurring biomaterials will accommodate the engineering of biomimetic materials. Biomimetics is the study of the structure and function of biological systems as models for the design and engineering of materials. Current research in biomimetics involves the synthesis of materials that function similarly to natural materials [1.18] including natural biopolymers, such as DNA and cytoskeletal proteins [1.19], and hard tissues, such as hydroxylapatite [1.19]. For example, bone was recently characterized for the development of new composite joint implant materials with comparable behavior to that of the natural bone [1.16]. Likewise, the toucan beak is a lightweight highly rigid

material that has been studied in the interest of replicating its unique mechanical properties. The beak is a highly organized cancellous bone fiber matrix, composed of a solid "foam" of airtight cells [1.19]. Also, replication of the surface chemistry of a lotus leaf offers excellent hydrophobicity and self-cleaning properties [1.19]. Effective engineering of biomimetic systems is largely dependent on thorough characterization of chemical and mechanical behavior of the naturally occurring biological system.

Also, mechanical and chemical properties are indicative of reliability of a material. Riggs and Melton recently confirmed that bone density is not the only factor contributing to osteoporosis [1.20-21], thus renewing interests in elastic modulus, strength, and toughness, with respect to biomaterial reliability. Surface chemistry may also improve the reliability of a material by providing a protective layer, such as sacrificial silicon oxide [1.22]. Establishing the properties of a biocomposite material as a function of various environmental conditions will allow for the development of a predictive model of material behavior. Such models may be useful for the refinement of treatments and processing techniques for biomaterials.

Though tremendous progress has been made, a better understanding of mechanical behavior and surface chemistry of biomaterials is still necessary. Characterization of naturally occurring biocomposites will allow for advancement of biomedical materials to control environmental response, the engineering of biomimetic materials in order to replicate natural biological materials, and the development of predictive models of the behavior of biological composite systems.

1.2 Research Intent

This research characterized the mechanical properties and surface chemistry of composite biomaterials in various environments using appropriate characterization techniques for the scale of the composites. The two biomaterial systems selected include the human tooth, composed primarily of hydroxylapatite and protein [1.23], and the Merino wool fiber, which belong to a class of proteins called α-keratins [1.24].

(I) Characterization of mechanical properties of dentin and enamel after common dental treatments and preparation for restorative procedures

Most of the published literature regarding mechanical properties of teeth do not consider affects of sterilization treatment, use internal controls, nor follow manufacturer recommended instructions [1.24]. Although some preliminary studies have been done on common dental treatments, including 30% hydrogen peroxide [1.23], there are no reports of the affect on these procedures on fresh teeth. The affects of increasingly popular whitening treatments and preparation for restorative procedures are still largely unknown [1.23].

(II) Determination of surface chemistry of Merino wool fibers

The composition of wool fibers is established; however, the distribution of these constituents has not been previously considered. The variation of surface charges along the surface of wool fibers was analyzed using force spectroscopy techniques. A better characterization of the wool surface will improve the quality and efficiency of fiber processing.

CHAPTER TWO

TEST TECHNIQUES APPLIED FOR BIOCHARACTERIZATION

2.1 Introduction

Analytical techniques that were originally developed for non-biological systems, including scanning electron microscopy, atomic force microscopy and nanoindentation, have proven effective for the characterization of biological materials. The application of these techniques requires appropriate considerations, including analytical models and testing parameters [2.1-3]. The application of effective investigative methods to biological systems is imperative to expanding the frontiers of biomaterials. This chapter will outline some characterization techniques used in the study of biocomposite systems.

2.2 Measurement of Small-Scale Structures by Nanoindentation

Mechanical behavior reflects the relationship between the deformation of a material and an applied load. Typically, mechanical behavior is described by properties including hardness (intrinsic resistance to plastic, or permanent, deformation), elastic modulus (intrinsic resistance to elastic, or recoverable, deformation) and strength (microstructure dependant resistance to failure). There are several acceptable techniques available for quantitatively determining elastic and plastic properties of bulk materials [2.4], such as tensile and microhardness tests. However, the small scale of many biological samples demands improved spatial, force and displacement resolution [2.5]. For investigations of mechanical properties of biomaterial composites, *e.g.,* the DEJ area of human tooth with an area of interest of ~200μm, nanoindentation is more appropriate.

Nanoindentation is an analytical method that has grown substantially in popularity due to its ability to spatially map the local mechanical properties of a surface [2.6].

During nanoindentation, a hard tip of known surface area and geometry is loaded into the sample, and then unloaded. The load and displacement are simultaneously monitored during loading and unloading. A typical load versus displacement curve is shown in Figure 2.1A. As the applied force is increased, the indenter tip moves into the material causing both elastic and plastic deformation. Plastic deformation from indentation can cause a permanent impression in the shape of the indenter tip, Figure 2.1B. When the load is removed, only the elastic deformation will recover [2.7].

Figure 2.2 is a schematic representation of a Triboscope™ spring-actuated nanoindenter [2.8]. A transducer is an electronic device that converts energy from one form to another. The type of transducer used in this research applies a load on the tip, which is proportional to the square of the voltage of the electrostatic energy generated between the middle plate and the upper and lower plates. The indentation depth of the tip is measured by monitoring the capacitance between the center electrodes and the outer electrodes. These tips typically have a radius of 0.3-10μm and are composed of hard materials, such as diamond or sapphire, to ensure that deformation occurs primarily in the specimens, rather than the tip. The geometries utilized include the Berkovich, conical, and cube-corner, each type inducing unique strain fields.

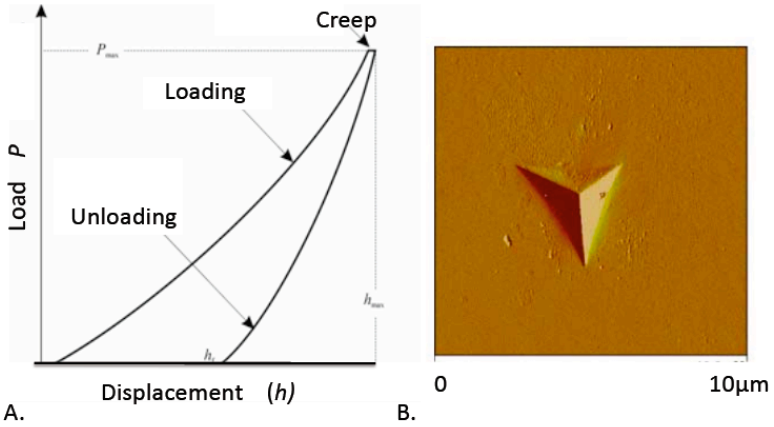

Figure 2.1: A plot of a typical load versus displacement curve [2.7] (A) and an image of residual plastic deformation expected to occur during nanoindentation [2.7] (B). Plastic deformation is the displacement that isn't recovered when the load is released, as indicated by the remaining impression of the indenter tip.

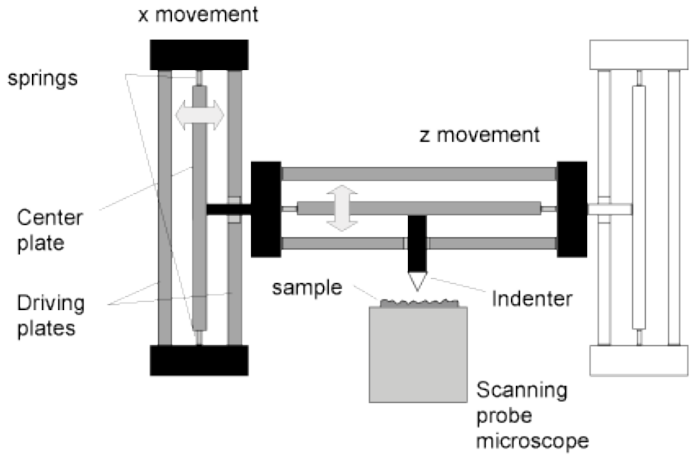

Figure 2.2: A schematic diagram of a Triboscope™ nanoindenter. This type of electrostatic system was used during the investigation described in this thesis, however electromagnetic transducer systems are also available [2.8].

Various models have been used to calculate the mechanical properties of a material from the unloading stiffness [2.9-10], specifically elastic modulus and hardness. Oliver and Pharr proposed the most prevalent method for homogeneous materials. They showed that the linear portion of the unloading curve (Figure 2.1A) indicates the

material's stiffness, S, as defined by:

$$S = \frac{2\sqrt{A_C}}{\sqrt{\pi}} E_r \qquad 2.1$$

where A_C is the contact area between the indenter tip and the sample and E_r is the reduced, or combined, elastic modulus. Figure 2.3 is a schematic diagram showing contact between the tip and sample, indicating the respective A_C and general region of plastic deformation.

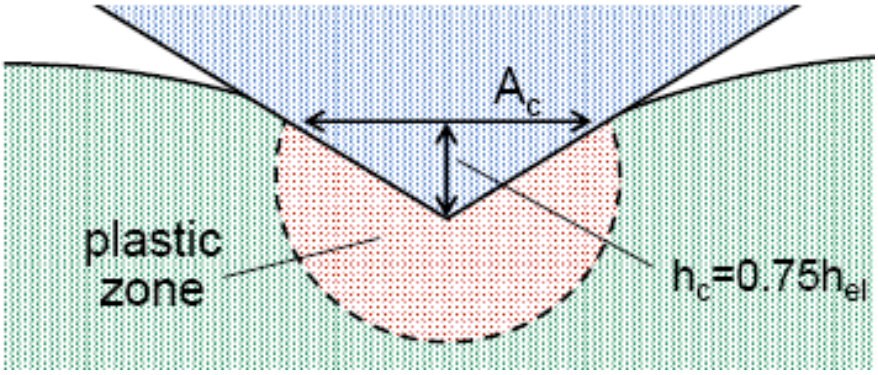

Figure 2.3: A schematic diagram of contact between a nanoindenter and material surface [2.7] where A_c is the contact area, h_c is the contact deformation, and h_{el} is the elastic deformation.

E_r is the combined average of the elastic moduli of the indenter tip and the sample. The reduced modulus can be used to calculate the sample elastic modulus (E_S):

$$E_s = \left(1 - \upsilon_s^2\right)\left[\frac{E_i}{1 - \upsilon_i^2}\right] - E_r \qquad 2.2$$

where E_i and ν_i are the elastic modulus and Poisson's ratio of the indenter tip respectively, and ν_s is the Poisson's ratio of the sample. Poisson's ratio is the elastic dimensional change occurring transverse to an applied uniaxial load, defined as:

$$\nu = -\frac{\varepsilon_x}{\varepsilon_y} = -\frac{\varepsilon_y}{\varepsilon_z} \qquad 2.3$$

A schematic illustration of the lateral and axial strains is shown in Figure 2.4 [2.4]. Poisson's ratio is an intrinsic property, and therefore does not vary significantly from bulk materials to thin films. Poisson's ratio is assumed to be the same for small scale and bulk measurements for many materials. For diamond indenter tips, as used in this study, the indenter modulus is 1141GPa, with a Poisson's ratio of 0.07 [2.8].

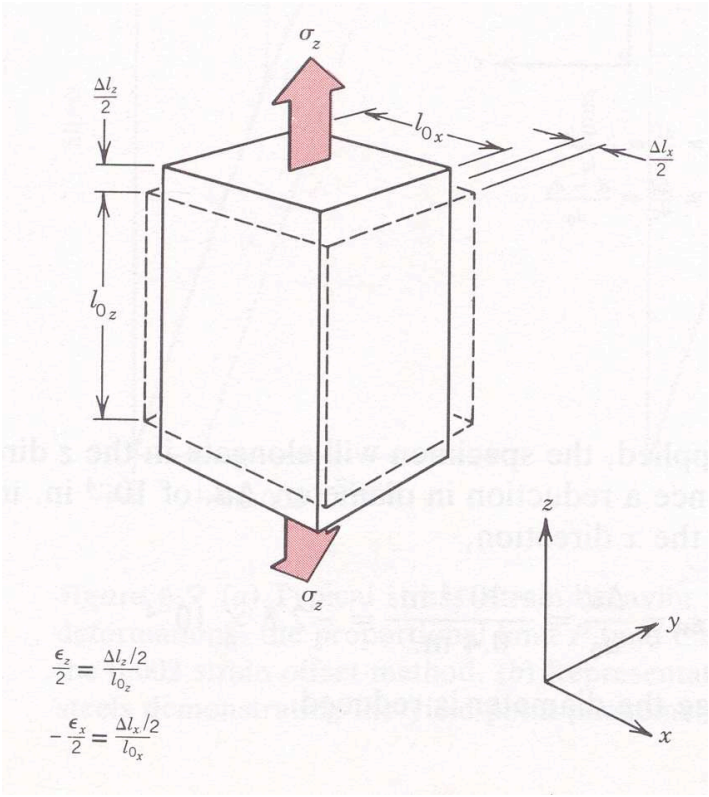

Figure 2.4: An illustration of strains used in calculation of Poisson's Ratio [2.4].

Hardness is another mechanical property that can be quantitatively measured using nanoindentation. Hardness is the measure of a material's resistance to deformation, determined quantitatively by:

$$H = \frac{P}{A_C} \qquad 2.4$$

where A_C is the contact area, and P is the maximum indentation load. During

nanoindentation, the load can be calculated by:

$$P = \alpha\left(h - h_f\right)^m \qquad 2.5$$

where h represents indentation depth, h_f represents the depth of residual impression after complete unloading, α is constant that depends on the mechanical properties of a specimen, and m is an empirical tip fitting parameter [2.7], equal to 2 for the conical indenter tips used in this study [2.8].

The average nanoindenter force ranges from 1μN to 500mN and displacement ranges from 1nm to 20μm [2.5]. The high sensitivity allows for investigation of fine-scale microstructures including thin films, nanowires, and biological structures [2.8]. Nanoindentation has been previously applied in studies of highly porous bioceramics [2.11] and scaffolds [2.12] for bone tissue engineering.

Biological materials introduce numerous analytical complications. Creep, the continued plastic deformation under constant stress, must be considered for some polymers and biological samples [2.5]. To reduce noise, Ngan *et al*. [2.13-15] and Cheng *et al.* [2.16] suggested sustaining the maximum load for a period of time, generally between 3 and 120 seconds, depending on the sample, to allow for creep to dissipate prior to unloading. This approach ensures that creep does not interfere with elastic modulus calculations, and has been effective for indentation of biocomposites, including bone [2.17] and dentin [2.18]. Environmental response and tip-sample interaction may also become an issue with biological materials [2.12]. Adhesion between the tip and sample may occur with some polymeric and soft tissue samples [2.19-22], often introducing error into analysis of mechanical properties. Adhesion is evident on the unloading section of a

load-displacement curve as a region of apparent negative load. Additionally, appropriate precautions should be taken to avoid contamination resulting from contact with biohazardous samples.

2.3 Atomic Force Microscopy

Atomic Force Microscopy (AFM) has been applied for generating force images related to the chemical nature of a surface, measuring topography of a non-conducting surface in a variety of conditions, [2.23-26] and sensing local mechanical properties of relatively soft elastic materials [2.27]. AFM is an imaging technique that employs a sharp tip (Figure 2.5) to scan across a sample surface. A schematic of the system is shown in Figure 2.6. A laser is reflected on the cantilever and then to a photodiode, monitoring the cantilever deflection as it bends in response to tip/surface interactions, into a photodiode [2.26].

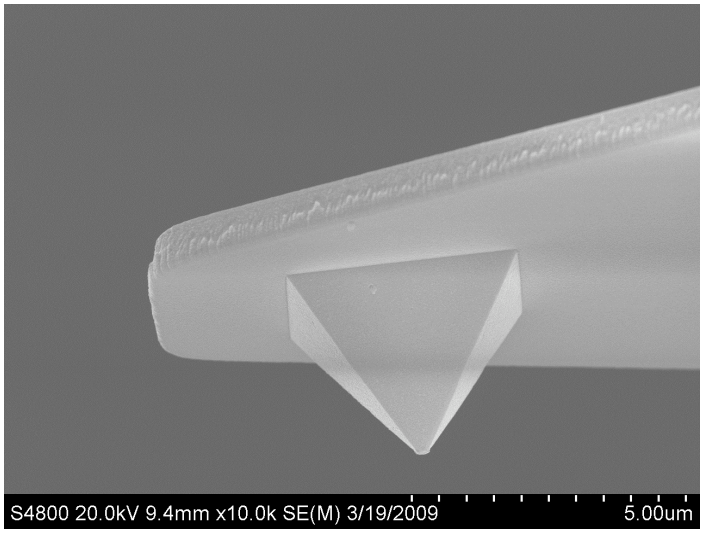

Figure 2.5: An SEM image of an AFM probe used in this study of surface charges on Merino wool fibers. SEM was used to determine the radius of the AFM tips for charge density calculations.

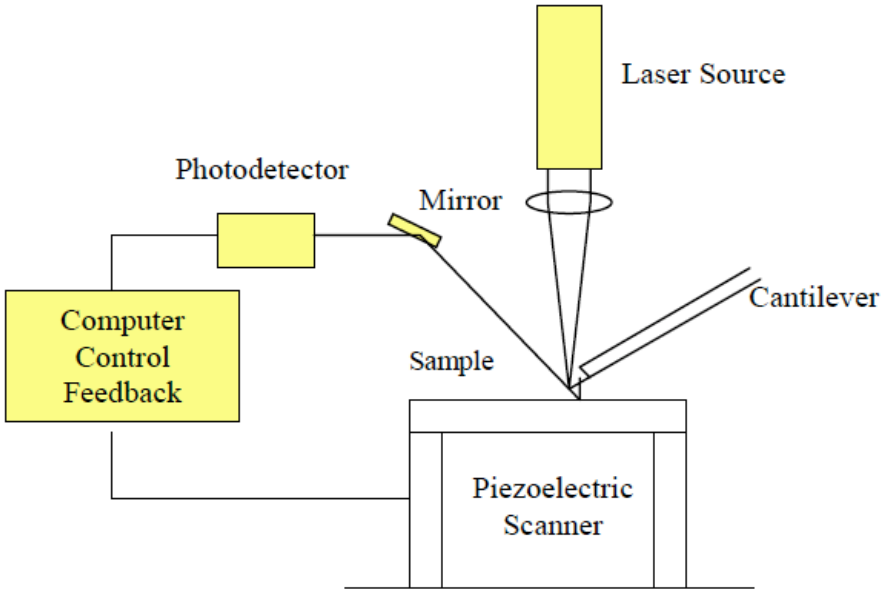

Figure 2.6: A schematic of image of an AFM [2.28]. Applying voltage to the piezoelectric tube controls samples movement. The tip is secured to the end of the cantilever. As the cantilever bends in response to the tip/surface interactions, a laser is reflected off the cantilever and into a photodiode.

Force microscopy is done in either contact mode, effective for determining surface roughness and structure, or tapping mode, used for force mapping in addition to imaging surface topography without inducing friction. In contact mode, also referred to as static mode, the tip scans along in close contact with the surface with a constant force between the tip and sample. In tapping mode, or dynamic mode, the cantilever oscillates, i.e. approaches and retracts from the surface repetitively during scanning rather than dragging along the sample. Tapping mode allows for monitoring repulsive and adhesive forces between the surface charge and the tip charge, to create maps of surface charges densities [2.29]. Initially, the tip is away from the surface, Figure 2.7A. As the tip approaches the surface, it will bend in response to long-range repulsive or attractive

forces, and bend, Figure 2.7B. The cantilever will continue moving toward the surface. When the set maximum force is reached, the cantilever will retract, Figure 2.7C. During retraction, the cantilever may detect adhesive interactions between the tip and the sample, Figure 2.7D. These bonds will break as the cantilever continues to withdraw, Figure 2.7E. At this point, the cycle may start again.

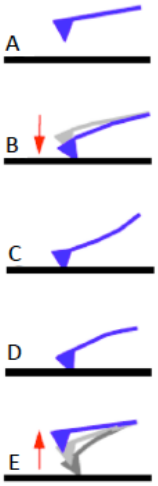

Figure 2.7: An outline of the steps involved in collecting data for a force curve. Initially, the tip is away from the surface (A). As the tip approaches the surface, it will experience long-range repulsive or attractive forces, and bend accordingly (B). The cantilever will continue moving toward the surface. When the set maximum force is reached, the cantilever will retract (C). During retraction, the cantilever may detect adhesive interactions between the tip and the sample (D). These bonds will break as the cantilever continues to withdraw (E)[2.28].

Hooke's law is used describe the interaction of the tip and sample. The force, F, is calculated as:

$$F = -kx \qquad 2.6$$

where k is the spring constant of the tip and x is tip deflection. Thermal tuning was used to determine the spring constant for each cantilever. The interaction between a probe of known charge and a sample is plotted, as deflection versus distance as the tip approaches

(extension) and withdraws from (retraction) the surface, Figure 2.8.

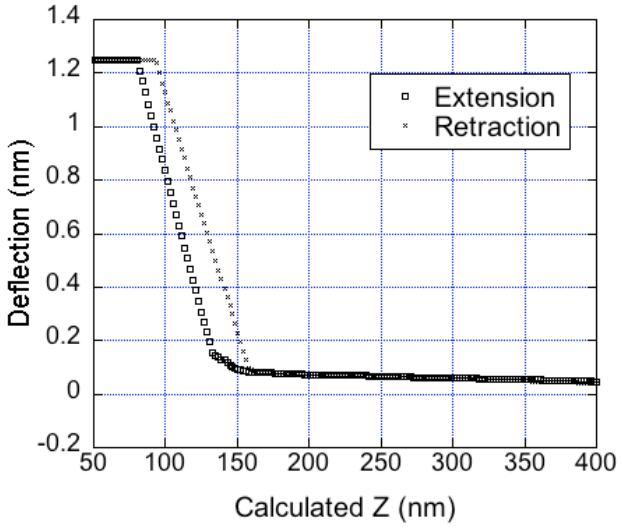

Figure 2.8: A representative deflection versus distance extension and retraction plot

Recent research has used AFM to expand the frontiers of biomaterials because of its capability to map soft, insulating samples in liquids with molecular resolution. For example, the recent analysis of the force interaction between bacteria and the silicon nitride surface of the AFM probe revealed that lipopolysacharides facilitate E. Coli adhesion to specific negatively charges surfaces [2.28], and AFM was used for the determination of the elastic modulus of naturally occurring biomaterials, *e.g.,* cells [2.30] and blood vessels [2.31].

Gibson *et al*. previously used force microscopy to characterize surface mechanical properties of Merino wool and, including elastic modulus [2.31-32]. However, the work in this thesis focuses on AFM to map surface chemistry variation along Merino wool (Figure 2.9) as a function of topography (Figure 2.10).

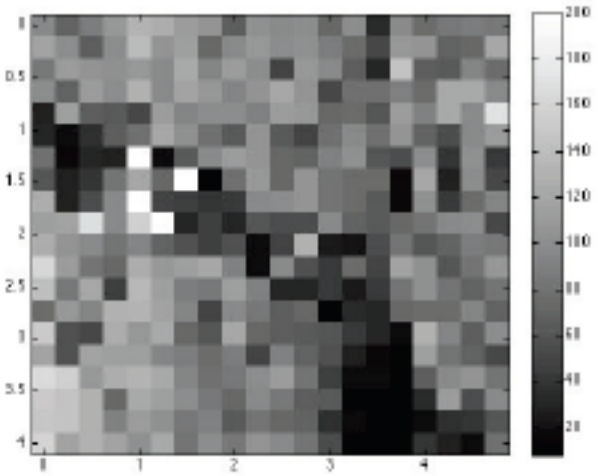

Figure 2.9: Illustrations of the use of AFM to create a map of surface charges. This charge map corresponds to the box of Figure 2.10.

Figure 2.10: An example of AFM being used to develop a topographical image of a sample surface. This particular sample is a wool fiber, including a scale edge, indicated by the box.

2.4 Scanning Electron Microscopy

Scanning Electron Microscopy (SEM) is a high-resolution imaging technique that uses a focused electron beam to generate signals containing information about a surface. The electrons' interactions with atoms on the sample surface typically result in secondary emissions from the specimen and the backscattering of electrons. A cathode ray tube displays the signal, indicating contrast within the image [2.33] that may reveal the texture, chemical composition, crystal structure and crystal orientation of the sample.

A schematic of a typical SEM is presented in Figure 2.11. As illustrated, an electron beam is produced as a voltage is passed through a filament, most commonly Tungsten or Lanthanum Hexaboride (LaB6), at the top of the column. The beam is attracted to the anode, condensed by a cylindrical magnetic aperture, and then focused by electromagnetic lenses. The sample chamber and electron beam column must be under vacuum to preserve the integrity of the beam.

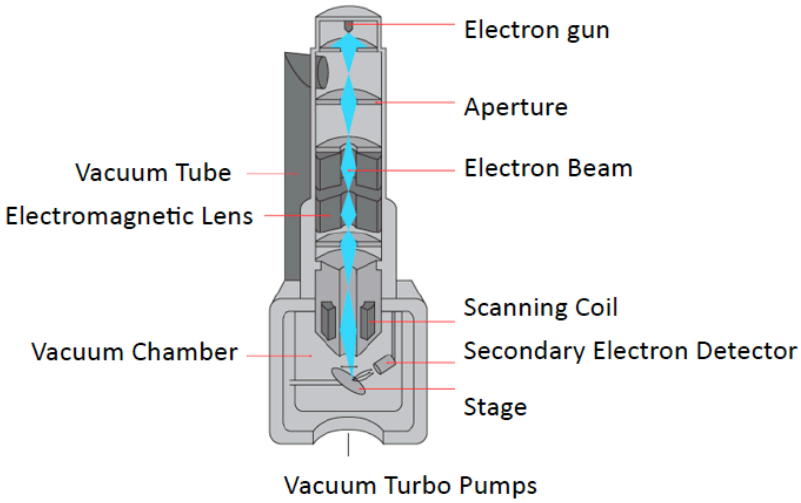

Figure 2.11: A diagram of the basic components of a SEM [2.35]. The sample is placed into a vacuum chamber. The electron gun at the top of the instrument produces an electron beam, which is condensed by the aperture and focused by electromagnetic lenses. The scanning coil rasters the beam across the sample as interactions between the beam and the sample are monitored.

To obtain an image of the sample, the electron beam scans the surface in a raster-like fashion. Scanning is possible by varying the current between two pairs of electromagnetic coils. As the electron beam strikes the sample, a photon and electron are emitted. Detection of electrons backscattered from the sample can produce a topographical image of the surface [2.33], Figure 2.12.

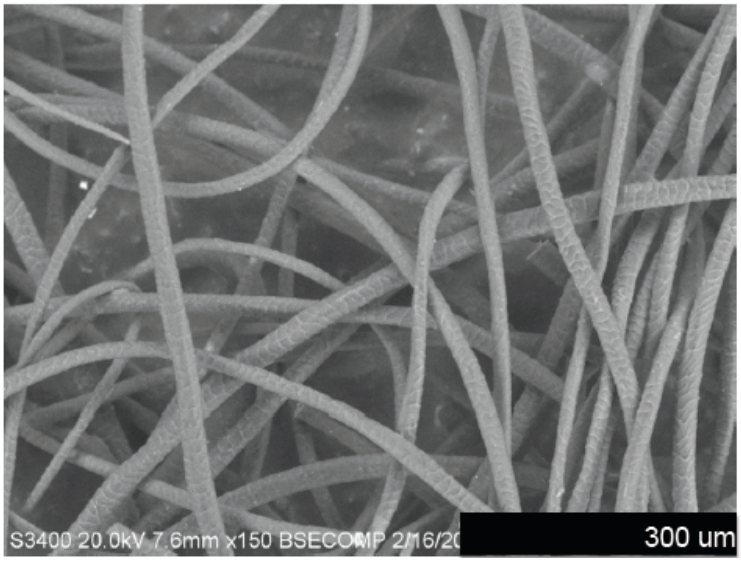

Figure 2.12: A SEM image of a merino wool sample. SEM provides improved resolution over optical microscopy.

Conductive samples are often better suited for SEM because the flow of electrons is unimpeded, thus build up of charge is less likely [2.34-35]. However, imaging of biological materials is feasible. Nonconductive samples may be coated in a thin layer of metal, *e.g.,* Au or Pl, by evaporating or sputtering. The application of a conductive coating will dissipate charge and prevent accumulation. Alternatively, a variable pressure or 'wet', low vacuum SEM maintains a high vacuum within the electron gun, but allows for a variable pressure in the sample chamber. This type of SEM is ideal for biological samples because charging is less likely, even on non-coated samples. [2.36-40].

2.5 Fourier Transform Infrared Spectroscopy

Fourier transform infrared (FTIR) spectroscopy is a means to identify a substance based on energy absorbed by chemical bonds within or on the surface of a sample. FTIR is convenient, relative to conventional infrared spectroscopy, due to the simultaneous

measurements of all resolution elements, and therein significant reduction of testing time. A Fourier transform is then used to convert the signal data into traditional IR spectra. The spectra allow for identification of chemical functional groups based on the specific frequencies of a molecule's vibration and rotation. FTIR has previously been used to distinguish between fluctuation in protein concentration in demineralized and restored dental enamel [2.41].

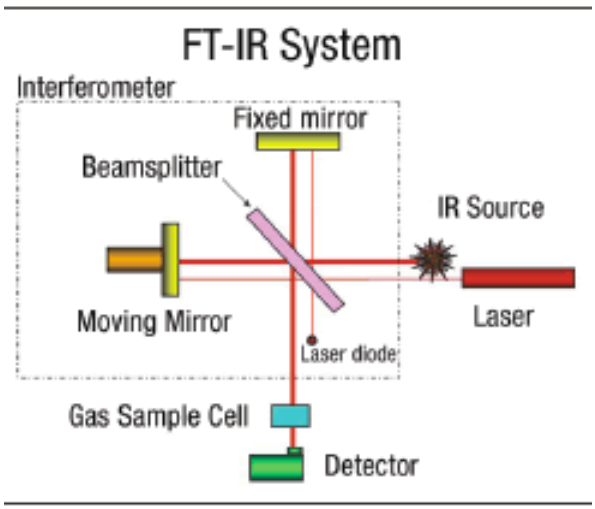

Figure 2.13: A schematic illustration of the experimental setup of FTIR [2.41]. An infrared beam is split into two beams. One is sent through the sample and the other is sent through a reference material. The beams are directed through a splitter that alternates which beam enters the detector.

Figure 2.13 outlines the general components required for FTIR. A Michelson interferometer functions by sending a parallel, polychromatic radiation beam to a beam splitter. The beam splitter is often composed of potassium bromide, or some other material that is transparent in the infrared region. The beam splitter reflects half of the light to a fixed mirror, where it is then sent back to the beam splitter. The remaining half of the light is reflected to a mirror that is constantly moving at a set speed, back and forth along a track. This light is also reflected back to the beam splitter. The light beams from

each mirror recombine and are reflected to the sample. The light that passes through the sample is focused on the detector, which processes the time domain signal changes from the interferometer modulation [2.41] to produce a spectrum, Figure 2.14.

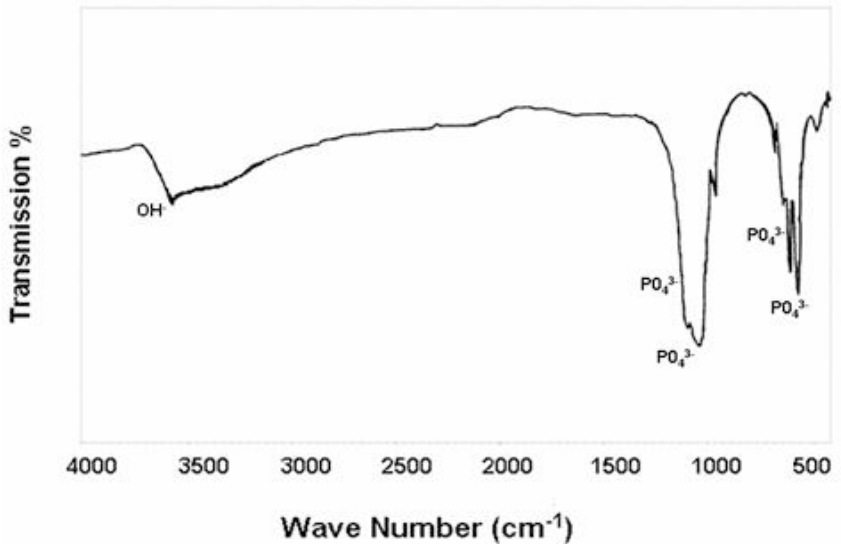

Figure 2.14: A FT-IR spectra of the apatite heated at 900°C for 3 hours [2.41].

IR spectroscopy is based on the relationship between intensity of transmitted and incident radiation, as defined by the Beer-Lambert law:

$$I = I_0^{-\varepsilon c l} \qquad 2.7$$

where I is the intensity of the transmitted radiation, I_0 is the intensity of the incident radiation, ε is the molar absorptivity, c is the concentration and l is the cell length. [2.42].

2.6 Fluorescence Microscopy

Fluorescence microscopy is similar in principle to conventional light microscopy, though it relies on the ability of certain molecules to emit light of a specific wavelength following the absorption of light of a higher energy [2.43]. The experimental setup is described in Figure 2.15. The sample of interest is labeled with fluorophores, and then illuminated with a high-energy source, typically Xenon or Mercury discharge lamps

[2.43]. The fluorescent species then emits light of a lower energy, producing a magnified image that is distinguishable from the original light source. Filters are used block radiation, permitting only the image of that which is fluorescing. An example of a fluorescent image is provided in Figure 2.16.

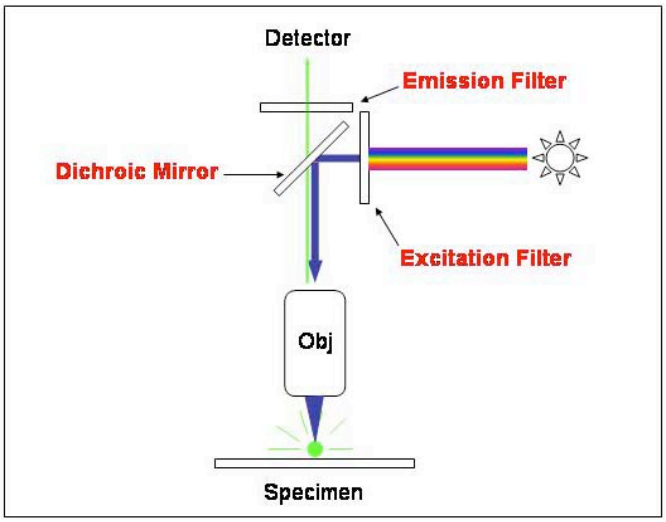

Figure 2.15: A diagram of the basic instrumental setup of florescence microscopy [2.45].

Though fluorescence microscopy may be used to specifically image specimens that have been marked with fluorescent tags, some materials naturally fluoresce, thus no additional fluorophores are required. Fluorescence microscopy is non-invasive and non-destructed, making it suitable for many biological samples, even living specimens [2.44].

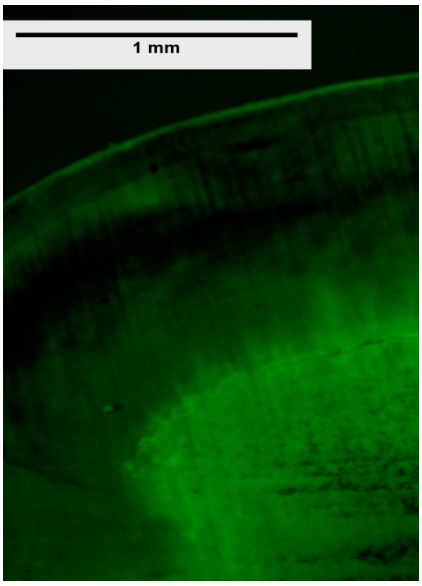

Figure 2.16: A fluorescence microscopy image of a tooth. The fluorescence shows the presence of Collagen Type 1, an auto-fluorescing protein that naturally abundant in teeth.

CHAPTER THREE

THE EFFECT OF TEETH BLEACHING AND PREPARATION FOR COMMON RESTORATIVE PROCEDURES ON THE MECHANICAL PROPERTIES OF ENAMEL AND DENTIN

3.1 Introduction

Biomimetic models uniting two dissimilar materials frequently motivate considerable interest in the mechanical properties of the human tooth [3.1]. Enamel is a hard substance, offering excellent wear resistance, located on the outside of the tooth (Figure 3.1). However just below the enamel, is dentin, a tough and highly elastic, thus effective for allowing stress to dissipate within the tooth. Both dentin and enamel are composed of hydroxylapatite, protein, and water, which are arranged in a porous matrix. Mature enamel is composed of 96% hydroxylapatite and 1% protein by weight, while dentin is composed of 70% hydroxylapatite and 20% protein. [3.3] SEM images of enamel and dentin may highlight the clear boundary between the two materials, known as the dentin-enamel junction (DEJ) (Figure 3.2). This DEJ is a highly specialized interface, transferring force between two materials of distinct mechanical properties, offering toughness and crack deflection. Crack propagation across the DEJ into the dentin is typically fatal to the tooth [3.4]

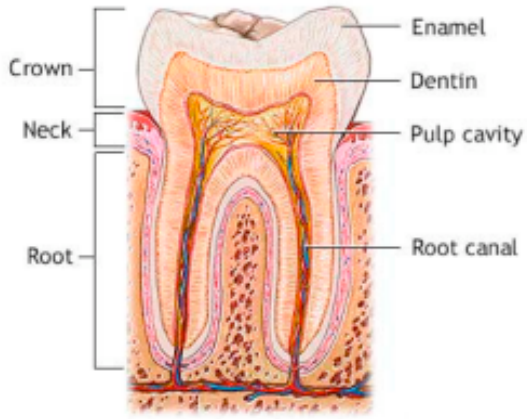

Figure 3.1: A schematic diagram of the components of a human tooth [3.2]

3.1.1 Background

The mechanical properties of dentin and enamel have been previously measured, as well as those across the DEJ [3.1, 3.6]. Variations in mechanical properties have been observed depending on the tooth type, tooth age, indent direction and environmental conditions [3.4-6].

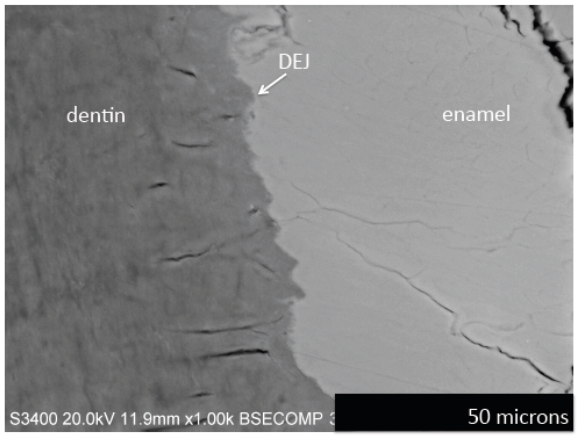

Figure 3.2: An SEM image of enamel, dentin, and the DEJ.

The reliability and longevity of a human tooth is controlled by many factors, including the mechanical properties of enamel and dentin and their composite structure. When these composite materials are subjected to dental treatments that alter the ratio of, or interface between hydroxylapatite and protein, the mechanical properties are also changed. Characterizing dentin and enamel will allow for the development of a better model to predict tooth response to altered environmental conditions, restorative materials, and preparation techniques and treatments used in dentistry.

3.1.2 Objective of the Problem-Hypothesis

Most previous studies of mechanical properties do not consider affects of sterilization treatment, do not use internal controls, nor follow manufacturer recommended instructions [1.7]. Previous studies of tooth structure by Finke *et al.* [3.8] and Hairul Nizam *et al.* [3.9] using nanoindentation have shown that external factors, such as exposure to soft drinks or 30% hydrogen peroxide [1.10], will change mechanical properties [3.11]. However, no work has yet measured the affects of increasingly popular

dental treatments of common clinical dental treatment procedures, such as whitening, or preparation for restorative procedures. This investigation will characterize the effect of these treatments on elastic modulus hardness and tracking changes in protein content.

Testing of teeth that have been subjected to autoclaving will permit comparison of mechanical property data values previously published in the literature. Characteristics of teeth that haven't been subjected to sterilization procedures, i.e. autoclaving and chlorine treatments may be more representative of natural conditions, and those which are not autoclaved have more clinical application. Each sample was compared to a portion of the same tooth, minimizing the affects of external factors, such as age of tooth, type of tooth, and health of the donor. Additionally, data analysis was done with the Oliver-Pharr model, which was often used in previous studies.

3.2 Experimental Procedures

The Medical University of South Carolina provided extracted human teeth. These teeth were obtained during necessary extractions due to vertical cracking or caries. It should be noted that areas in the vicinity of defects were not tested in this research.

Both whole and sliced teeth were stored in Hank's Balanced Salt Solution (HBSS) prior to testing. Previous studies have shown that HBSS does not to affect the mechanical properties of teeth during long-term storage [3.1, 3.6-7, 3.12].

Samples for nanomechanial testing are sensitive to storage and handling procedures. A significant loss of hardness was observed when samples were stored in the presence of the metal sample puck used for AFM testing. This was potentially due to breakdown of the hydroxylapatite matrix (Figure 3.6) [3.13]. Previous studies by

Gustafason *et al.* indicated that calcified tissues are sensitive to mineral content [3.13]. Furthermore, Habelitz *et al.* showed that storage solution can create an electrical potential that will demineralize teeth and lead to softening [3.1]. Therefore, all the results reported here are those of teeth stored in HBSS and only mounted on pucks immediately prior to testing.

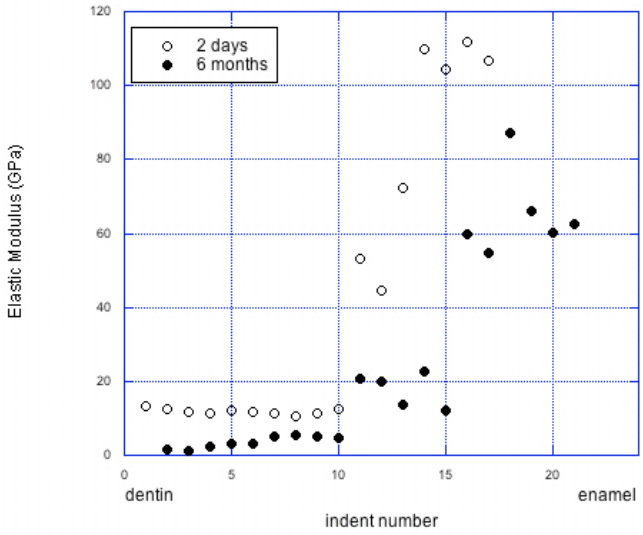

Figure 3.3: An illustration of the significant loss of mechanical integrity accompanying long-term storage in HBSS while mounted to AFM puck.

A subset of the teeth was disinfected using chlorine treatment and autoclaving, while others received neither sterilization treatment, Table 3.1. Treatments were applied to teeth following manufacturer recommended instructions (e.g., only the exterior surface of the teeth were treated). Changes in material properties were then monitored across the DEJ. Teeth were sectioned to allow for direct comparison, reducing variation due to prior condition of the tooth.

	Autoclaved	Non-autoclaved
Crest Whitestrips™	✔	✔
Opalescence™	✔	✔
UltraEtch™	✔	✔

Table 3.1: Chart of environmental conditions to which samples were exposed prior mechanical testing. Three teeth were sterilized and received one of the dental treatments, Crest Whitestrips™, Opalescence™, or UltraEtch™. Three other teeth were not sterilized but did receive one of the three dental treatments.

3.2.1 Sample Preparation

The teeth were briefly air dried, then subjected to one of three surface treatments groups Table 3.1. Prior to sample preparation, each tooth was divided in half, with one half of the tooth receiving treatment, while the other half served as a matched control. Sample treatment and preparation is outlined in Figure 3.4 A and B. As directed by the manufacturer's instructions, one group was treated with 35% phosphoric acid (UltraEtch™) for 30 seconds, the second group was coated with 20% carbamide peroxide (Opalescence™) and wrapped in Parafilm™ for one hour, the third group was wrapped in Crest Whitestrips™ Premium, 10% hydrogen peroxide, for 30 minutes.

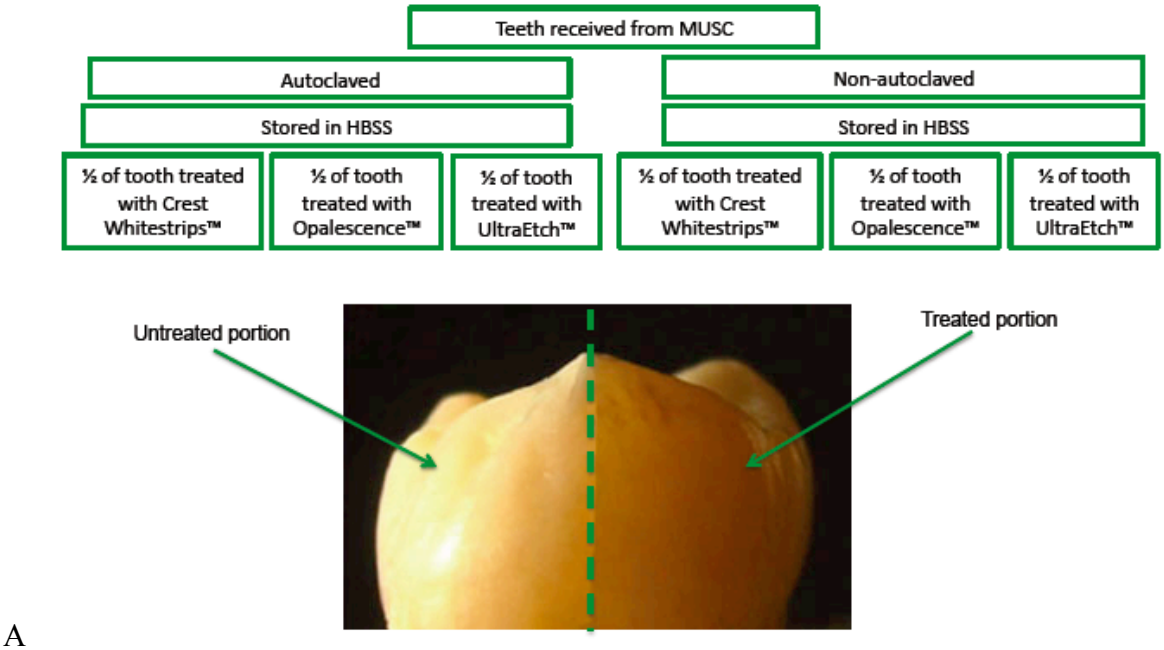

A

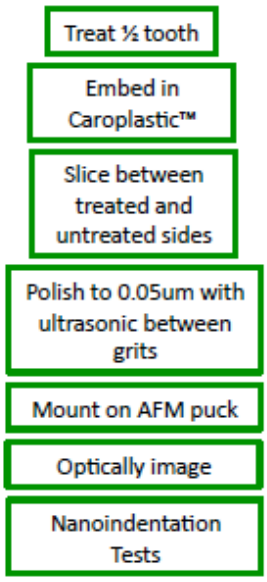

B

Figure 3.4: A flowchart of the tooth sample treatment (A) and preparation process (B).

After each treatment, the teeth were rinsed with water. The teeth were then embedded in Caroplastic™, a non-infiltrating polyester resin, to allow for easier handling during polishing. Caroplastic™ does not alter the mechanical properties of the sample

[3.14]. After the manufacturer recommended curing time of approximately 24 hours, the teeth were sliced with a 0.8mm thick diamond saw into ~2mm sections. Each slice was prepared according to a previously established method for nanoindentation of teeth [3.7]. Polishing was done with silicon carbide paper (Buehler) in the following progression: 400 grit for 1 minute, 500 grit for 5 minutes, 600 grit for 8 minutes and 5μm polishing paper (K4000 from Exakt) for 10 minutes. Then the slices were fine polished with 0.05μm alumina slurry for 30 minutes [3.7]. Between each polishing step, the slices were ultrasonically cleaned in deionized water for 10 seconds [3.7]. A short ultrasonic time was necessary to remove residual particles from the polishing. Polishing reduced the depth of the section that may have been subjected to thermal damage from slicing sufficiently so that undamaged areas analyzed during testing.

Each sample was then mounted such that the untreated and treated pairs reflected similar orientation to control the effects of tubule direction. Consistency in sample preparation was critical, particularly regarding slicing direction and tubule alignment. This internal comparison minimized the effect of preexisting condition of the sample. [3.10]. Each tooth was optically imaged to ensure that there were no features that might not be an ideal representation of enamel or dentin and to achieve consistent testing location between a sample and it's respective control (Figure 3.5). Samples with apparent cracks, cavities, fillings, etc. were eliminated from the study.

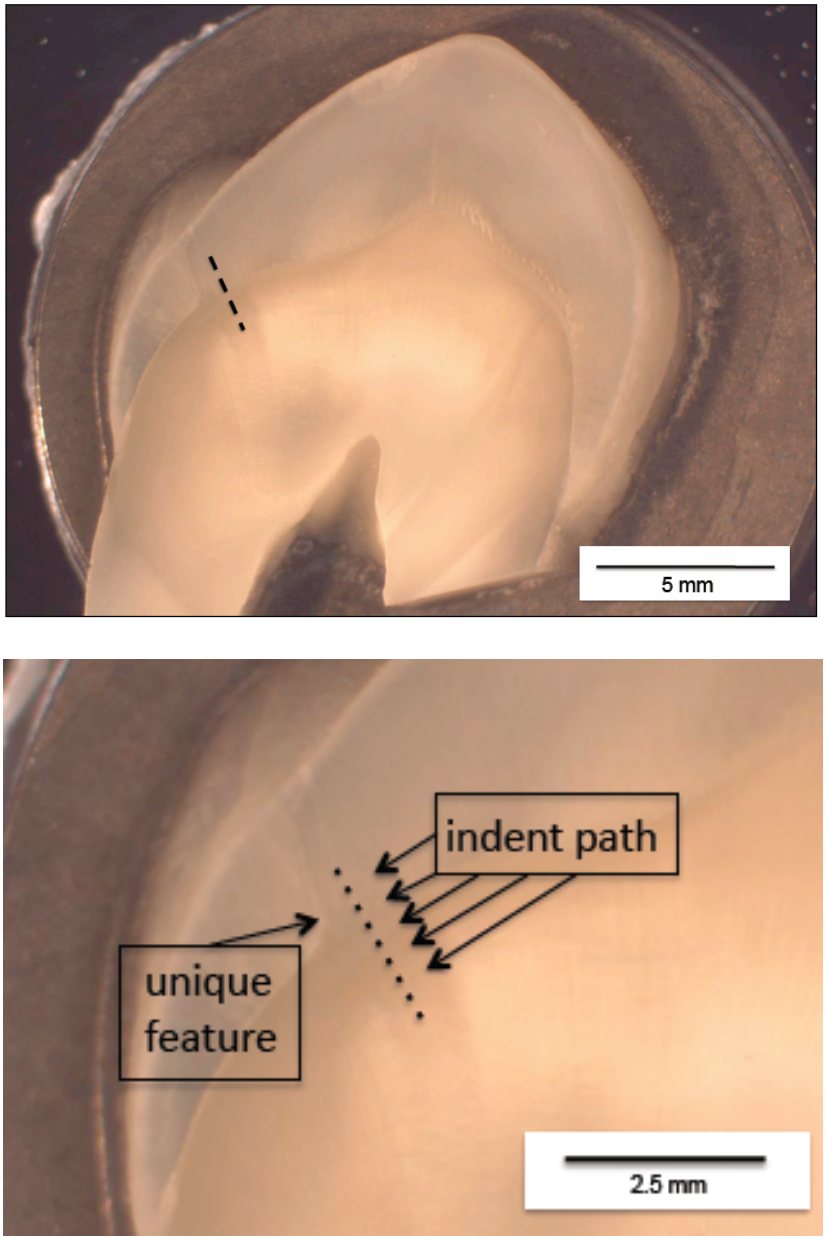

Figure 3.5: An optical image of sliced tooth allows for more consistent indent area selection. When possible, distinct features were identified to serve as a reference location for aligning the sample in the nanoindenter. Thus improving uniformity of tubule direction between samples.

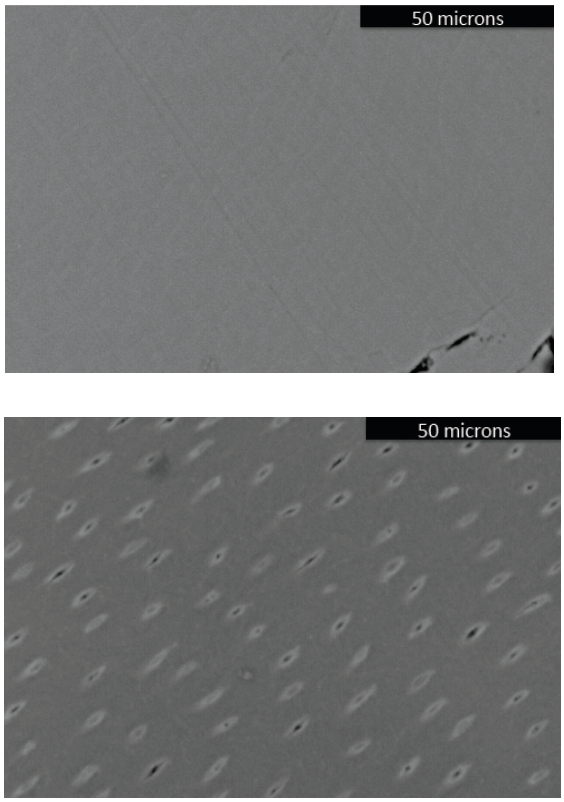

Figure 3.6: Backscatter SEM images of dentin (A) and enamel (B) that has been subjected to 1 minute of ultrasonic cleaning. There seems to be a loss of integrity of the dentin tubules.

3.2.2 Sample Characterization

Initial studies using backscatter SEM revealed that extended ultrasonic times disturbed the mineral structure, specifically, resulting in a collapse of tubule (Figure 3.7). Habelitz [3.5] made mention of a similar finding, noting that ultrasonication longer than 30 seconds may alter the surface enamel's mechanical behavior. Ultrasonic cleaning for 10 seconds was sufficient to remove polishing particles while not disrupting dental structure and properties. The tooth slices were easily broken free from the Caroplastic™ after polishing. Finally, each slice was etched with 0.005 mol% citric acid for 5 seconds, and then rinsed with deionized water. The tooth slices were stored in HBSS until mechanical testing.

Characterization of the effects of the whitening agents and phosphoric acid etching was accomplished by nanoindentation, atomic force microscopy (AFM), optical imaging, fluorescent microscopy, scanning electron microscopy (SEM), and Fourier

transform infrared spectroscopy (FTIR). These techniques were discussed in greater detail in Chapter 2.

3.2.3 Mechanical Properties

Nanoindentation was performed using a Hysitron™ quasi-static transducer with a modified Veeco Multimode™ AFM. The indentations transected the DEJ, as shown in Figure 3.7, with a 2 micron 90° conical, diamond tip, similar to the tip used in previous nanoindentation of teeth [3.15]. Each indent was performed under a constant loading rate of 1200μN/sec with 10μm spacing between indents to prevent effects of plastic deformation of previous indentations. A hold segment was enforced to allow for creep relaxation, which may occur in soft, biological samples.

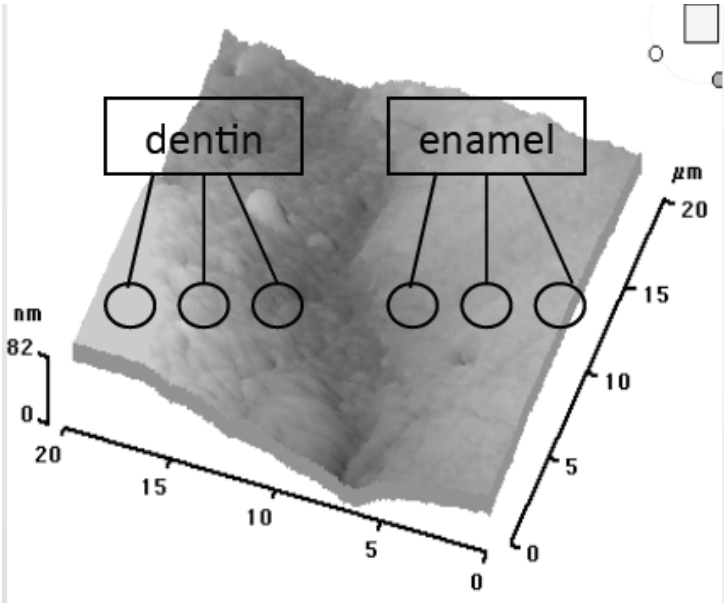

Figure 3.7: An AFM image of the indentation pattern, moving from the dentin across the DEJ and into the enamel.

3.2.4 Roughness

AFM was performed on tooth slices before and after etching and whitening treatments with and without polishing to verify that indentation depth was sufficient to overcome affects of surface roughness. Contact AFM with a Veeco™ NP non-conductive silicon nitride tip was used to map out the topography of the DEJ and images were analyzed to determine RMS roughness of untreated samples and those treated with Opalescence™ or UltraEtch™.

3.2.5 Composition

Chemical characterization was done to establish a correlation between the mechanical properties and composition. Samples were treated and prepared as described in Table 3.2. FTIR was employed to further analyze apparent changes in composition. The exteriors of autoclaved teeth were treated with Crest Whitestrips™, Opalescence™ or UltraEtch™ according to the package directions, or left untreated. Dentin was separated from the enamel, formed into potassium bromide pellets then analyzed by IR spectroscopy under dry nitrogen.

Fluorescence microscopy was used to image the protein content of teeth with exposure to Crest Whitestrips™, Opalescence™ or UltraEtch™. The most abundant protein in teeth is Type I collagen, which autofluoreses at approximately 550 nm when excited in the 470–490 nm wavelength [3.14-15]. Four teeth were prepared for examining autofluorescence. The exteriors of three autoclaved teeth were treated according to the manufacturer recommended directions and one was left untreated. The samples were then sliced longitudinally into 2mm sections.

Tooth Treatment	FTIR	Autofluorescence	Monoclonal Anti-collagen
No treatment	✔	✔	✔
Autoclaving & Crest Whitestrips™	✔	✔	
Autoclaving & Opalescence™	✔		
Autoclaving & UltraEtch™	✔	✔	
Crest Whitestrips™ of ½ tooth			✔
Opalescence™ of ½ tooth			✔
UltraEtch™ of ½ tooth			✔
Autoclaved as whole tooth			✔
Autoclaved as whole tooth and secondary autoclaving after slicing			✔
Hydrogen peroxide treatment of ½ tooth			✔

Table 3.2: Chart of preparation methods for compositional testing. Three teeth were sterilized and received one of the dental treatments, Crest Whitestrips™, Opalescence™, or UltraEtch™. Three teeth were not sterilized but did receive one of the three dental treatments. One tooth was autoclaved prior to slicing. One tooth was autoclaved prior to slice and again after slicing. One tooth was treated with hydrogen peroxide.

To further clarify is there was a loss of collagen Type 1 with treatment, it was useful to use fluorescence microscopy for samples stained with monoclonal anti-collagen Type 1. An additional batch of teeth was prepared. Non-autoclaved teeth were bisected, with half treated with Crest Whitestrips™, Opalescence™, or UltraEtch™, while the other half of each tooth was untreated. To further isolate the effect of hydrogen peroxide, the active ingredient in Crest Whitestrips™, a slice of a non-autoclaved tooth was soaked in 3% hydrogen peroxide for 30 minutes. Additionally, one tooth that had been autoclaved prior to slicing, and one tooth that had been autoclaved both prior to slicing

and after slicing were stained to evaluate the affect of autoclaving on chemical composition. Rhodamine was elected as a secondary antibody to distinguish between selective binding and the autofluorescence of collagen in the green spectrum. These observations further characterized dental proteins' response to whitening and etching.

3.3 Results and Discussion

Variation of hardness and elastic modulus within both the enamel and dentin of different teeth was investigated by means of quasi-static nanoindentation. Nanoindentation data were analyzed according to the Oliver-Pharr model, as described in Chapter 2, which assumes that there is no pile-up of material around the indent. Preliminary tests indicated that the respective load for nanoindentation of dentin and enamel yielded no noticeable pile-up, Figure 3.8 A and B.

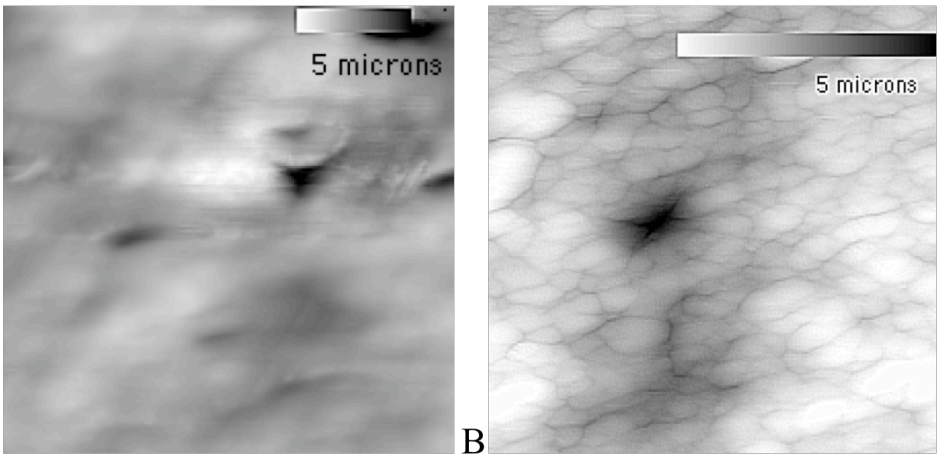

A B

Figure 3.8: AFM images of nanoindentation into enamel with a Berkovich tip (A) and dentin with a conical tip (B) indication the absence of pile-up.

The Oliver-Pharr Model also assumes homogeneous deformation in the area below the indenter tip [3.18]. Enamel and dentin have tubules which are oriented

approximately perpendicular to the direction of indentation. However, the small size of the indent relative to the inter-tubule spacing validated the assumption of homogeneity. A topographical image of the area around the indentation area was obtained prior to indentation, and efforts were made to avoid indentation into a pore or void to prevent breaking the indenter tip and allow the sample to be treated as a uniform material. The maximum area of contact, $A_{c\ max}$ was calculated to be approximately 2.5μm^2 according to the average dentin indentation depth, at which the tip is assumed to be spherical. The deformation zone is 2-3 times A_c, small relative to the spacing between pores, ~50μm^2 [3.7] [3.19]. Thus, the modulus and hardness represent those of the hard material between the pores, and will not be affect by the presence of pores located away from the indentation area.

3.3.1 Mechanical Properties of Autoclaved Samples

For the untreated group, subjected to autoclaving, the average elastic modulus of dentin was 31.63±6.58 GPa and enamel was 111.71±16.02 GPa (Figure 3.9). The hardness value for dentin was found to be 0.99±0.30 GPa and that of enamel was 4.35±0.38 GPa, Figure 3.10. These values are consistent with those of previously published studies, in which elastic modulus of enamel was found to be 70-120 GPa [3.6] and hardness is 3-6 GPa, [3.10-11, 3.20-25], while the elastic modulus of dentin was reported to be 16-37 GPa with hardness of 0.74-1.09 GPa [3.26-33]. Untreated teeth exhibit similar trends in elastic modulus and hardness across the DEJ, though there is fluctuation among teeth, possibly due to age of tooth, location of tooth, or type of tooth [3.22]. To account for these variations, each

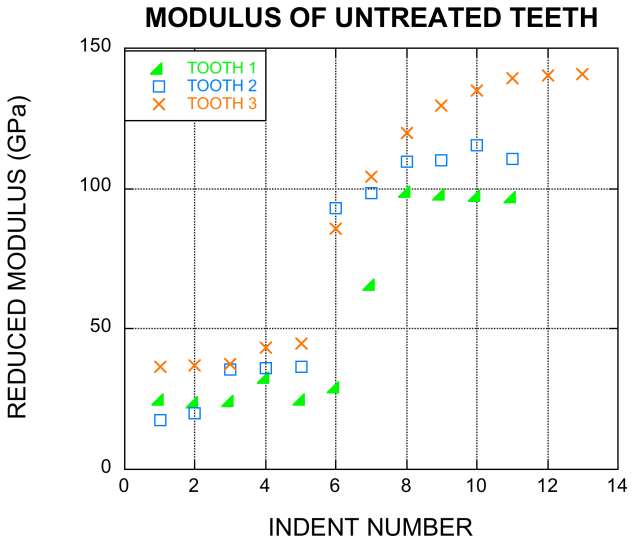

Figure 3.9: An illustration of the general trend and variation among the elastic moduli of untreated teeth.

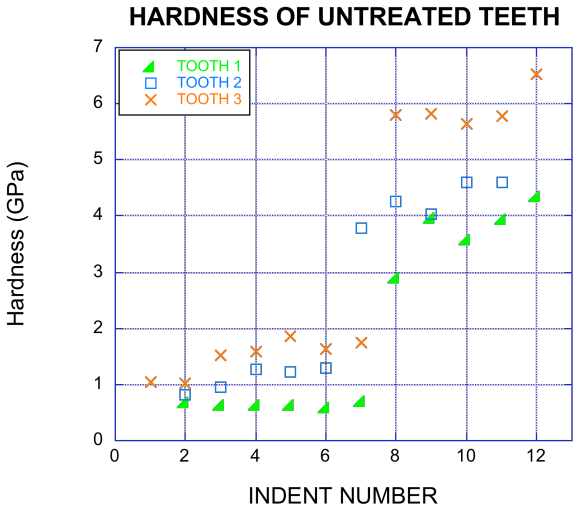

Figure 3.10: An illustration of the general trend and variation among the hardness of untreated teeth.

test was conducted on a single tooth that was sectioned to allow for comparison of treatment and control.

The enamel and dentin elastic modulus and hardness of teeth treated with the Crest Whitestrips™ were significantly increased (p=3.3E-4, p=9.8E-6, p=4.3E-4 and p=9.8E-6 respectively), as highlighted in Figure 3.11-14.

Whitening of autoclaved teeth due to Opalescence™ decreases modulus of dentin (p=0.0079) but has no significant effect on enamel (p=0.308>0.05), though only the exterior enamel was treated. Treatment with Opalescence™ also resulted in a decrease in the hardness of dentin (p=6.9E-3).

Etching with UltraEtch™, 35% phosphoric acid, did significantly decrease the modulus and hardness of enamel (p=1.4E-3, p=0.14E-2 and p=2.0E-3) and the modulus of dentin, but did not significantly change the hardness of dentin (p=0.132) for autoclaved teeth.

3.3.2 Mechanical Properties of Non-autoclaved Samples

Teeth that did not receive the autoclaving and chlorine sterilization demonstrated lower elastic modulus and hardness. Treatment of non-autoclaved teeth with Crest Whitestrips™ resulted in a significant decrease in the elastic modulus and hardness of enamel (p=5.8E-3 and p=4.9E-3) and increase in that of dentin (p=4.7E-2). Treatment of non-autoclaved teeth with Opalescence™, (Figure 3.11-14), resulted in a decrease in elastic modulus of the dentin (p=1.3E-2), though the hardness of dentin, as well as hardness and modulus of enamel remained unchanged (p=0.461, p=0.406, and p=0.168 respectively). Treatment of non-autoclaved teeth with UltraEtch™ resulted in a decrease

of modulus and hardness of dentin (p=1.0E-3 and p=3.4E-3) and enamel (p=1.2E-6 and p=1.8E-2), as evident in Figure 3.11-14.

The changes in hardness and modulus with treatments may be the result of a combination of the protein loss, apparent in Figure 3.16, and the effect of fluoride, an additive in Crest Whitestrips™, suspected to offset the effects of the peroxide. The phosphoric acid, which was applied for only 30 seconds, may not have penetrated to the dentin, which could explain the more pronounced decreased hardness of enamel, relative to the dentin (Figure 3.13 A). FTIR may be used to further investigate this theory by monitoring the rate and extent of etchant penetration into the tooth.

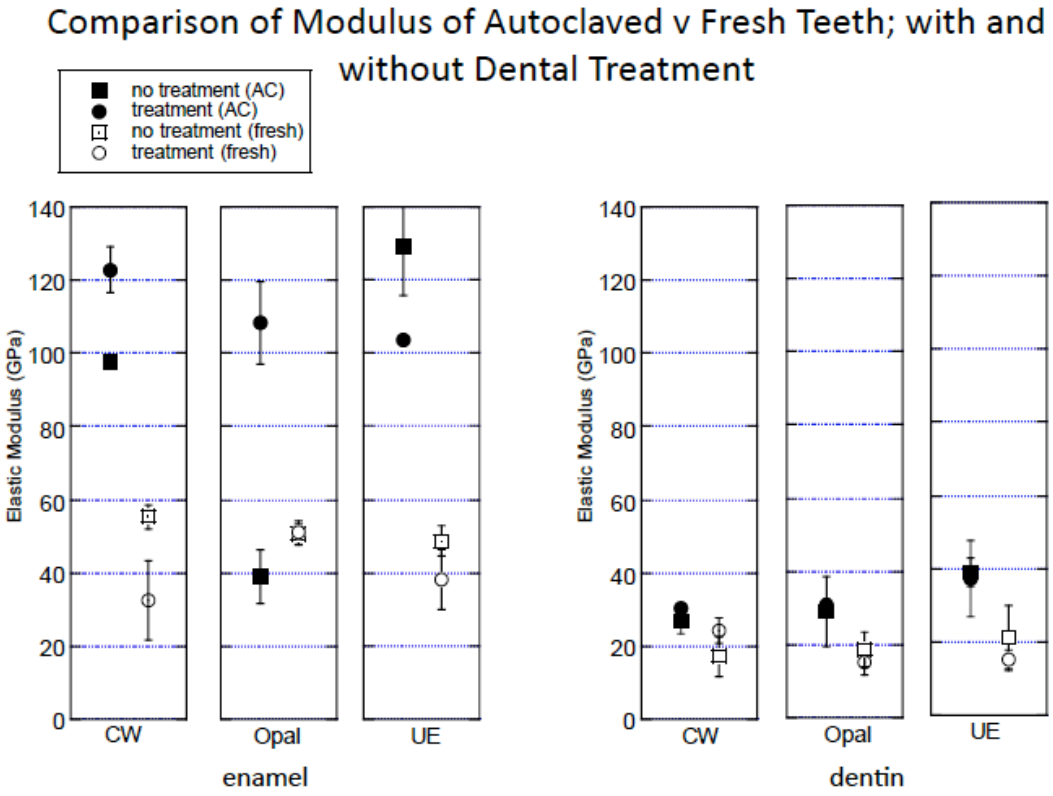

Figure 3.11: A direct comparison of the elastic modulus of fresh teeth and those that have been autoclaved, upon treatment with common dental agents. Autoclaving tended to increase the elastic modulus of enamel and dentin. Crest Whitestrips™ treatment of autoclaved teeth increased the modulus of dentin and enamel. Opalescence™ treatment of autoclaved teeth didn't significantly change the modulus. Treatment of autoclaved teeth with UltraEtch™ reduced the modulus of enamel and dentin. Crest Whitestrips™ treatment of non-autoclaved teeth increased the elastic modulus of dentin and decreases the elastic modulus of enamel. Opalescence™ treatment decreased the modulus of dentin. UltraEtch™ treatment decreased the elastic modulus of dentin and enamel of non-autoclaved teeth.

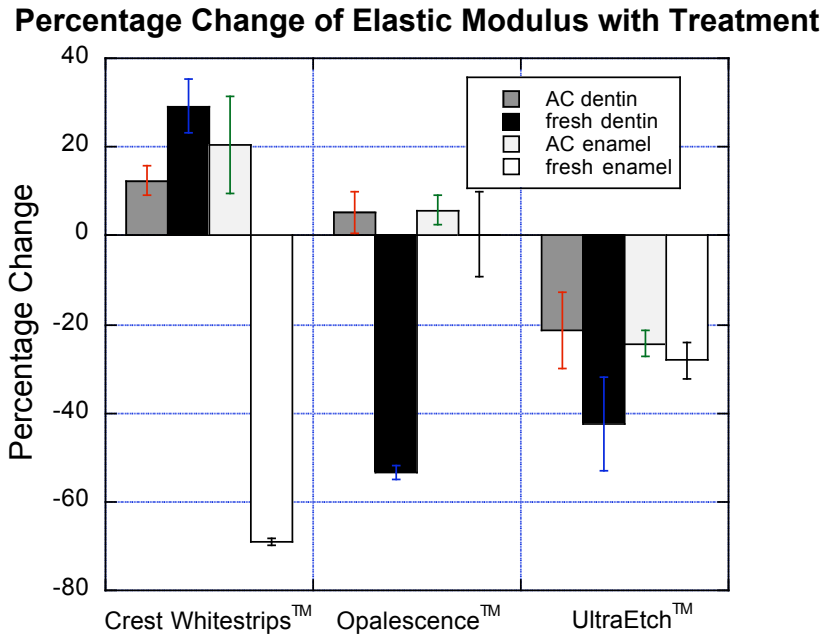

Figure 3.12: The observed the percentage changes in elastic modulus with each treatment.

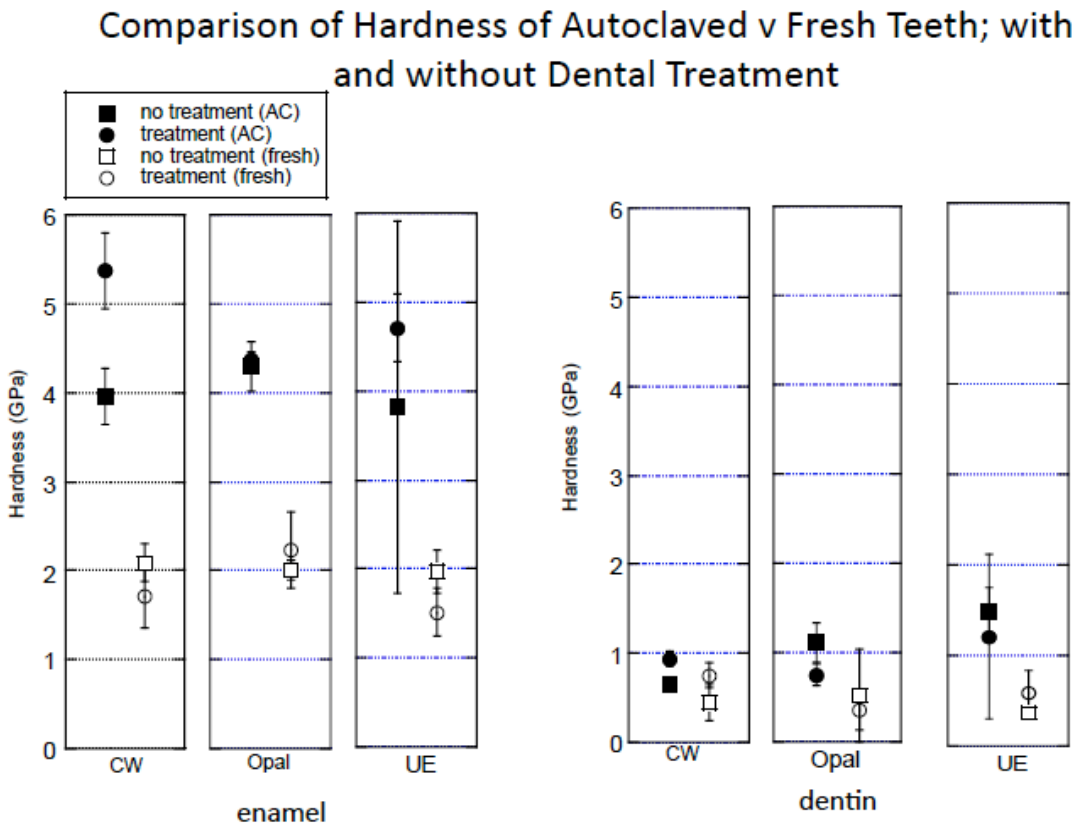

Figure 3.13: A direct comparison of the hardness of fresh teeth and those that have been autoclaved, upon treatment with common dental agents. Autoclaving tended to increase the hardness of dentin and enamel. Autoclaved teeth treated with Crest Whitestrips™ showed an increase in the hardness of dentin and enamel. Those treated with Opalescence™ showed a decrease in hardness of dentin. Autoclaved teeth treated with UltraEtch™ demonstrated a reduction in the hardness of enamel. Non-autoclaved teeth demonstrated a decrease in hardness of enamel and an increase in the hardness of dentin with Crest Whitestrips™ treatment. Opalescence™ treatment didn't change hardness significantly. UltraEtch™ treatment decreases the hardness of enamel and dentin.

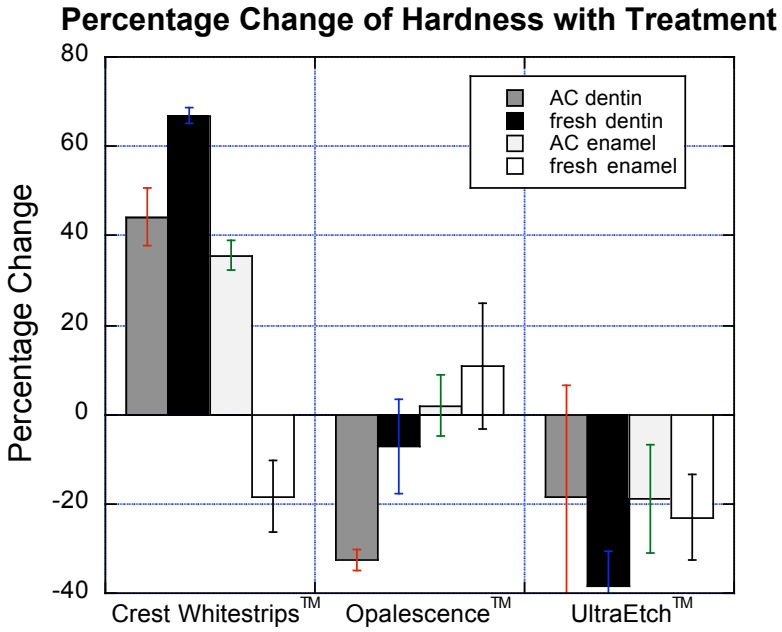

Figure 3.14: The observed the percentage changes in hardness with each treatment.

3.3.3 Roughness

AFM was used to determine the roughness of dentin and enamel before and after treatment with UltraEtch™. AFM revealed that RMS roughness of enamel increased from 12.97±7.34 nm to 342.92±106.95 nm and dentin increased from 21.10±9.95nm to 165.99±70.86nm due to etching with 35% phosphoric acid ($p<<0.01$, Student's t-test). These initial values are comparable to those published [3.10], and the trend of change with treatment is as predicted, based on treatments with lesser concentrations and similar application of phosphoric acid [3.31].

AFM was also used to determine the effect of treatment with Opalescence™ (Figure 3.15 B) on dentin and enamel. AFM indicated that whitening with Opalescence™ did not significantly change the RMS roughness of enamel ($p=0.057>$, Student's t-test),

but did significantly increase the RMS roughness of dentin from 16.93±5.12nm to 22.06±5.98nm (p=4.2E-7, Student's t-test).

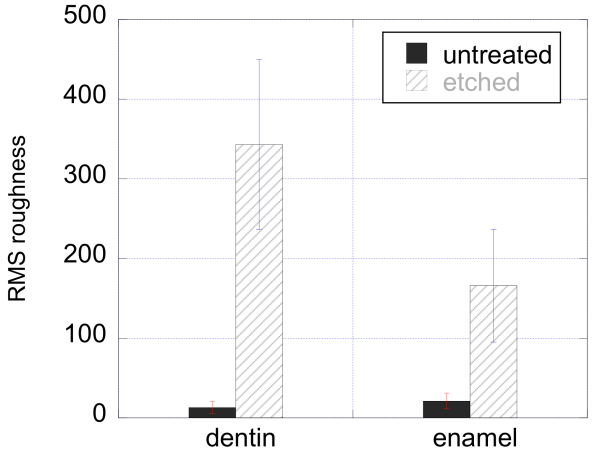

A

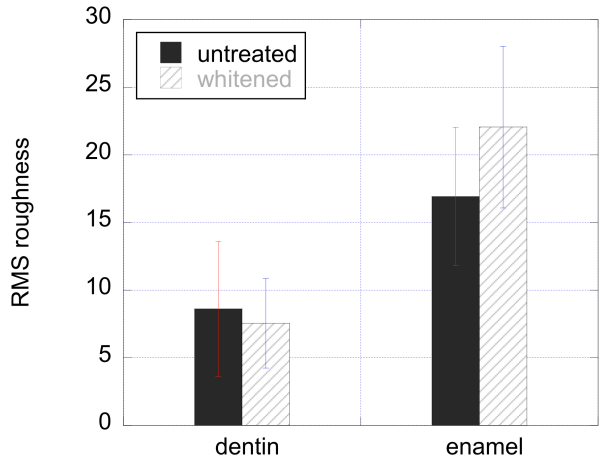

B

Figure 3.15: A comparison of RMS roughness of untreated tooth versus an UltraEtch™ treated tooth (A) and an versus an untreated tooth Opalescence™ whitened tooth (B) over an 80μm x 80μm area.

3.3.5 Composition

Fluorescence microscopy indicated a reduction in the protein concentration of teeth subjected to various treatments. Protein concentration was further investigated by means of Fourier transform infrared spectroscopy, Figure 3.16. FTIR has been used for comparing protein levels in natural and deproteinated dentin and enamel [3.30] [3.31], and may be indicative of the effect of dental treatments on teeth Analysis of IR spectra of dentin revealed notable changes in amide bonds with dental treatments, thus indicating a possible loss of protein with treatment. However, further research is necessary to investigate the denaturing of proteins that may be apparent in altered absorbance at other wavelengths.

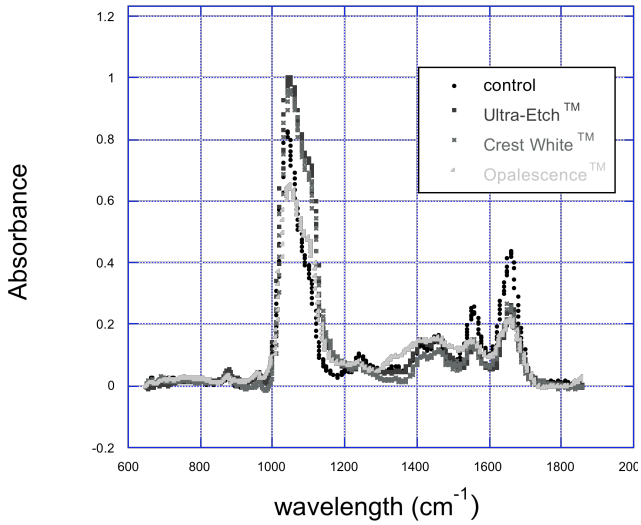

Figure 3.16: An FTIR spectra of teeth subjected to various treatments indicates a reduction of phosphate and carbonate, and amide bonds, further suggesting a loss of protein with treatments

Florescence microscopy in the green spectrum showed a loss of collagen in teeth that were treated with Crest Whitestrips™ and UltraEtch™ compared with those that were not treated. Figure 3.17 shows loss of fluorescence along the DEJ with Crest Whitestrips™ treatment and a loss of fluorescence within the dentin with UltraEtch™ treatment. Denatured collagen may also autofluorese.

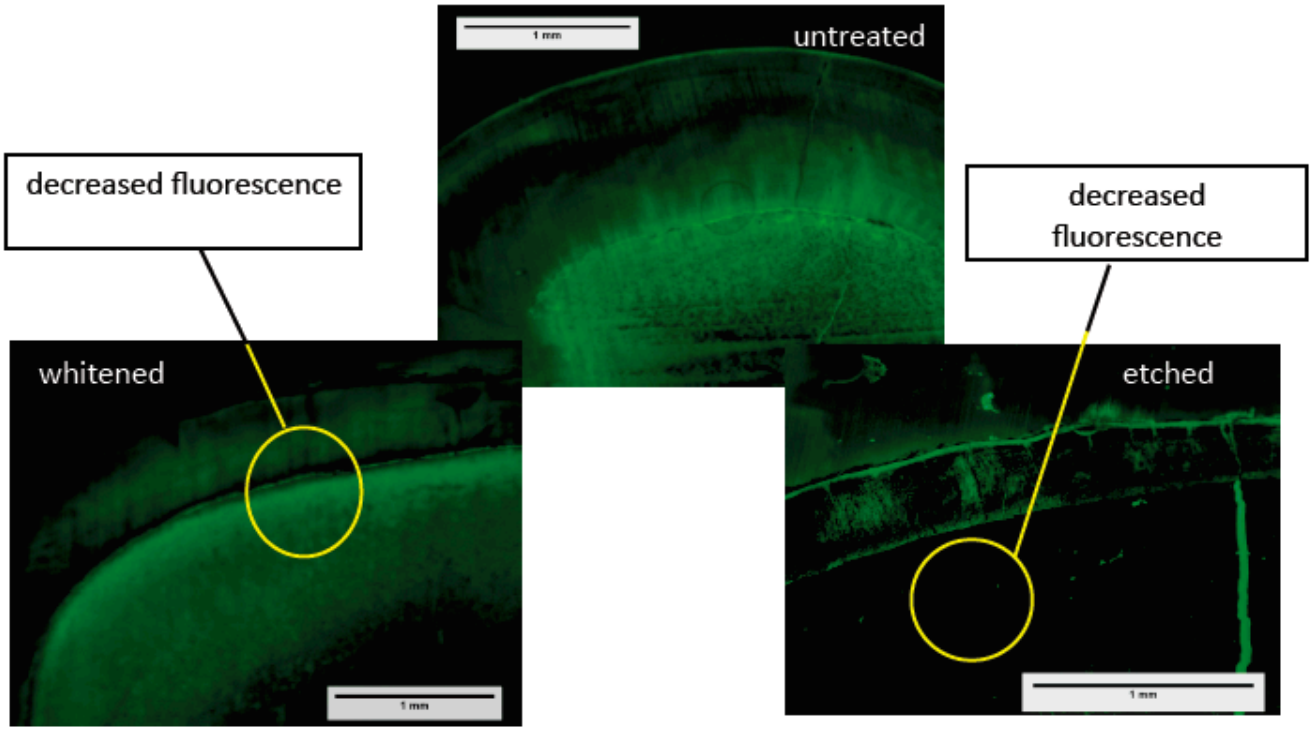

Figure 3.17: A collection of florescent microscopy images of an untreated tooth, a tooth treated with Crest Whitestrips™, and a tooth treated with UltraEtch™. There appears to be a loss of fluorescence along the DEJ with Crest Whitestrips™ treatment and a loss of fluorescence within the dentin with UltraEtch™ treatment.

Florescence staining of intact collagen type 1 with monoclonal anti-collagen Type 1 indicated the presence of proteins in Figure 3.18, highlighting the apparent overall loss of collagen and increased definition of DEJ, which accompanies treatment with Crest Whitestrips™ (Figure 3.18 B). There is a loss of collagen in the outer enamel of teeth treated with Opalescence™ (Figure 3.18 D). There is also a noticeable loss of collagen in the dentin and enamel and increase definition of the DEJ in those teeth that have been etched with 35% phosphoric acid (Figure 3.18 F). An overall loss of florescence was observed with hydrogen peroxide, the active ingredient in Crest Whitestrips™, treatment (Figure 3.18 I). The secondary autoclaving causes an additional overall loss of

florescence and increased definition along the DEJ (Figure 3.18 J and K). This lack of protein is most obvious on the surface of the enamel teeth dental treatment.

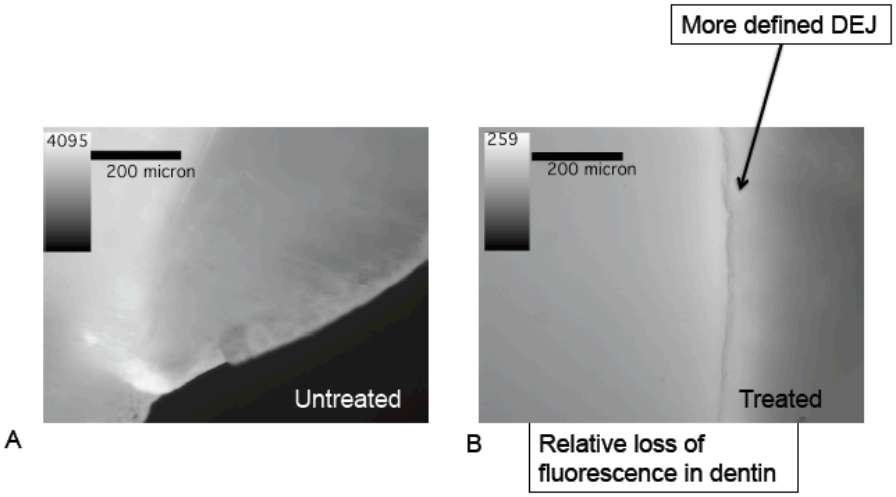
More defined DEJ
4095
200 micron
Untreated
A
259
200 micron
Treated
B
Relative loss of fluorescence in dentin

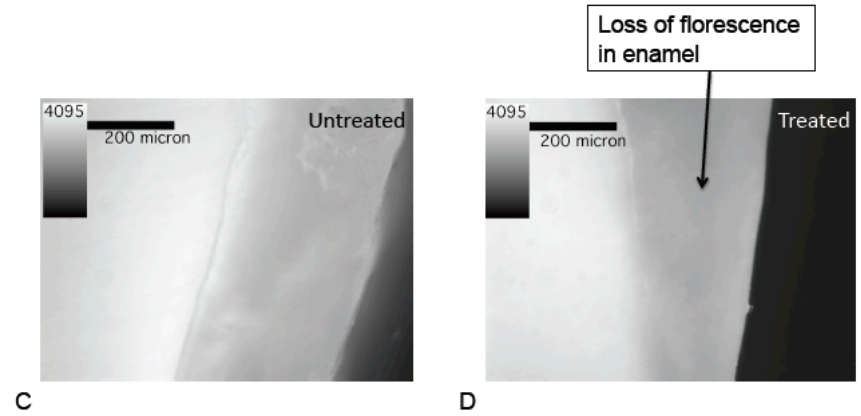
Loss of florescence in enamel
4095
200 micron
Untreated
C
4095
200 micron
Treated
D

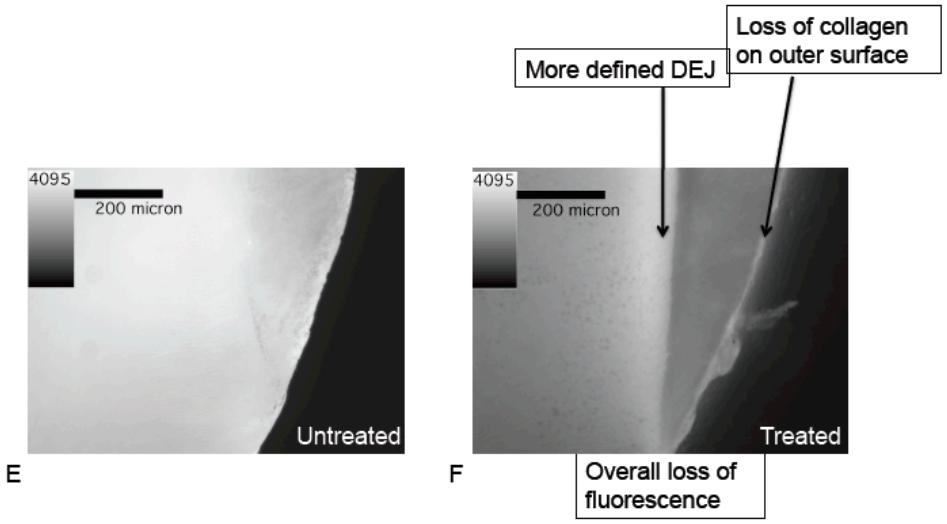
Loss of collagen on outer surface
More defined DEJ
4095
200 micron
Untreated
E
4095
200 micron
Treated
F
Overall loss of fluorescence

(Continued from previous page)

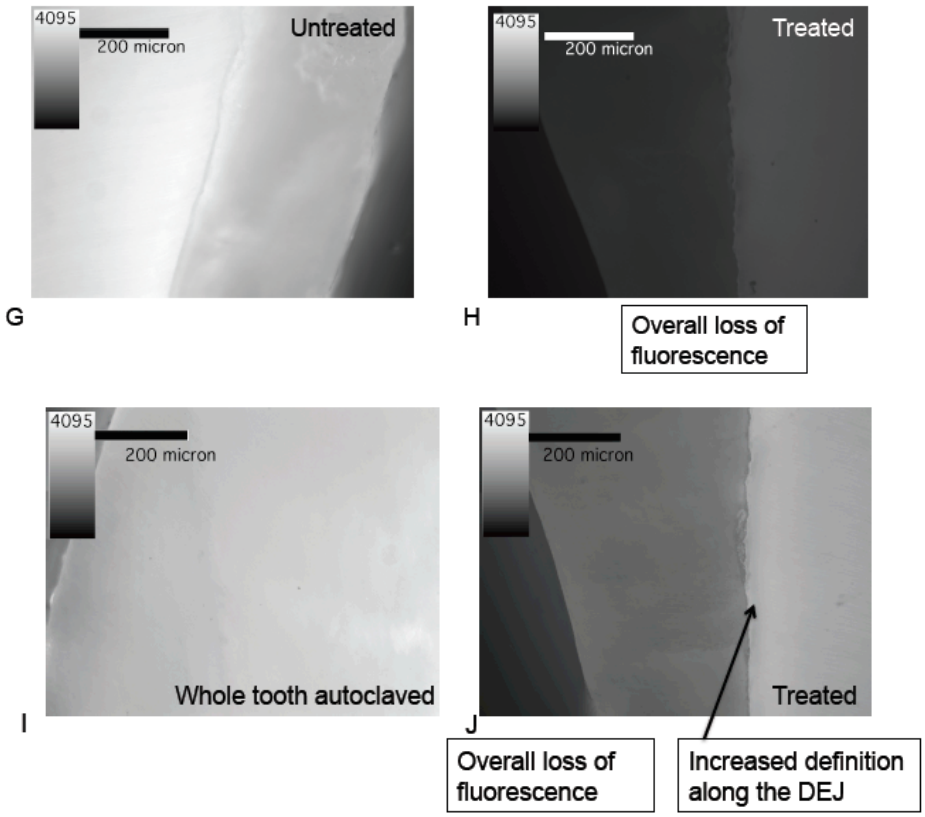

Figure 3.18: A collection of florescent microscopy images of teeth treated with Crest Whitestrips™ (Figure B), Opalescence™ (Figure D), UltraEtch™ (Figure F), as well as the untreated portions of the same teeth (Figure A, C, and E respectively). Figure H shows a florescent image of a tooth treated with hydrogen peroxide, and the corresponding untreated tooth, Figure G. Also shown is a tooth subjected to autoclaving as a whole tooth, Figure I, and a tooth subjected to an additional autoclaving after slicing, Figure J.

3.4 Conclusion:

Development of a standard testing technique is warranted for tooth preparation (enamel and dentin), storage and testing. Autoclaving was generally found to increase the elastic modulus and hardness of teeth. Although only surface of each tooth was treated, changes were noted in both the enamel and dentin. Whitening due to Crest Whitestrips™ increases elastic modulus and hardness of enamel and dentin of autoclaved teeth.

Whitening due to Opalescence™ decreases hardness of dentin but has no significant effect on enamel of autoclaved teeth. UltraEtch™ significantly decreases elastic modulus and hardness of enamel and decreases the elastic modulus of dentin of autoclaved teeth. Treatment of non-autoclaved teeth with Crest Whitestrips™ resulted in a significant decrease in the modulus and hardness of enamel and increase in the hardness and modulus of dentin. Treatment of non-autoclaved teeth with Opalescence™ resulted in a decrease in dentin elastic modulus. Treatment of non-autoclaved teeth with UltraEtch™ resulted in a significant decrease in modulus and hardness of enamel and dentin. Changes in mechanical properties of teeth may be due in part to the loss of protein, evident with optical imaging, fluorescent microscopy, and FTIR.

3.5 Future Work

With a new understanding of tooth response to environmental conditions during common dental treatment, it is possible to develop a synthetic dental material that will respond more like natural tooth. Uniformity across the biological material/synthetic material interface will promote effective transfer of forces when subjected to the forces of mastication.

Additionally, research is underway, as described in Appendix B, to establish the dental pulp cell response to substrate topography. Consideration of surface features and replication of natural mechanical properties may allow for optimal bioresponse, improving the design of biomaterials for cranial reconstruction.

CHAPTER FOUR

MAPPING OF CHARGES ALONG THE SURFACE OF WOOL FIBERS

4.1 Introduction

Sheep wool offers unique advantages for use in high-performance and multi-climate apparel, bedding and carpets, as well as medical garments [4.1]. The fiber is durable, inherently antimicrobial, and offers superior temperature regulation, moisture wicking and breathability.

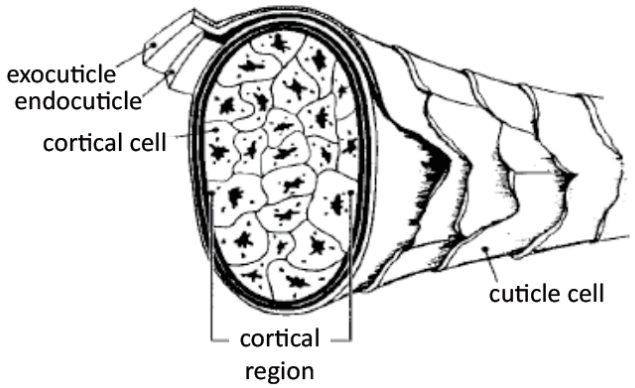

Figure 4.1: A schematic diagram of a wool fiber showing its heterogeneous structure [4.2].

Wool structure is complex, as shown in Figure 4.1, with heterogeneous composition of proteins, primarily, and lipids [4.3]. These fibers have spindle shaped cortical scales, which are staggered along the fiber length as shown in Figure 4.2. In woven fabrics, these scales result in the ratcheting effect observed during agitation [4.4].

The overall surface charge of wool fibers is established and frequently considered in the development of dyes. Additionally the amino acid components of wool fibers have been determined by protein assays, x-ray photoelectron spectroscopy, and Fourier transform Raman spectroscopy [4.5-8]. However, the arrangement of these amino acids along the surface has not been previously determined. More clarification of the charge distribution on the surface of wool fiber will improve processing and treatments.

4.1.1 Objective

The objective for this project was to determine the distribution of amino acids along the wool fibers. At a pH of 6, comparable to the pH at which the experiments in this paper were carried out, the zeta potential for the wool fibers was found to be -24 mV [4.9]. This indicates a slightly negative charge over the entire surface of the wool [4.10].

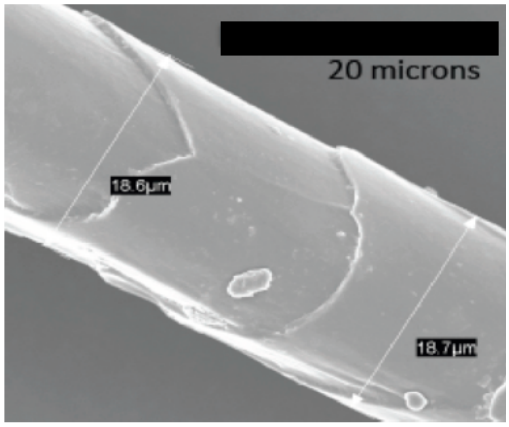

Figure 4.2: An illustration of scales along a merino wool fiber, shown to occur at regular intervals in this SEM image. The scale ridges are approximately 500nm in height and each scale is spaced around 20 µm apart.

The functional groups of several of the amino acids in wool are charged. Negatively charged groups include aspartic and glutamic acids, while positively charged groups include lysine and arginine. Also, cysteine is present in significant quantities in wool fibers, and may also be distinguishable with the detection of sulfhydryl group interactions.

This study mapped the amino acid distribution on wool fiber surfaces with respect to topographical features using chemically specific high-resolution [4.9-16]. Atomic Force Microscopy has previously demonstrated adequate force sensitivity in an electrolytic fluid to permit the measurement of electrostatic interactions between the tip and the sample [4.10]. Force measurements differentiated between types of amino acids based on charge interactions between the wool fiber surface and the AFM tip, with nanometer resolution. Measurements were also acquired under elevated pH to more

specifically distinguish the force contribution of particular types of amino acids. Observation of the binding sites of nanoparticles targeting specific chemical groups was used to verify the results of the AFM investigation.

4.2 Materials and Experimental Plan

4.2.1 Tip Preparation and Force-Distance Experiments

Merino wool fibers were scoured according to standard industrial procedures and mounted onto Atomic Force Microscope (AFM) pucks with cyanoacrylate epoxy. The samples were then were placed in 0.0015M phosphate buffer solution within the fluid cell of a Dimension 3100 Veeco AFM. A total of twenty fibers were prepared, with each experiment performed on a unique scale.

High resolution force spectroscopy experiments were performed using Au-coated Si_3N_5 cantilevers (Veeco Probes, nominal k~0.12N/m and R_{tip}~50nm) that were chemically functionalized with a self assembled monolayer (SAM) of 10mM 11-mercaptoundecanoic acid to create negatively charged carboxyl-terminated, 10mM 11-Amino-1-undecanethiol to create positively charged amine-terminated probes, or 100mM dithiolthreitol (DTT) to create sulfur sensitive probes. Probes were then rinsed with and stored in ethanol. Tips were rinsed with 0.15M Phosphate Buffered Saline (PBS) immediately prior to use.

20μm x 5μm contact-mode imaging scans with constant displacement velocity of 1 mm/sec were used to image the fiber morphology. Using the "Point and Shoot" feature of Veeco Nanoscope™ v6 controller software, normal force versus tip-sample separation distance was measured every 250 nm in an evenly spaced 5μm x 5μm grid centered over

the scale edge. Three individual approach curves were taken at each grid location to obtain a representative average value for the charge at that location. This gave 1,200 force-distance curves per scale for each of the 20 scales analyzed. The spring constant for each cantilever was measured using the thermal tune feature of the Veeco Nanoscope™ software. The radii of representative AFM probes were determined using SEM. The mean radius was assumed to be consistent for all AFM probes in the research.

4.2.2 Estimation of Surface Charge Density from Carboxyl/Amine/Sulfide Force-Distance Curves

The force-distance curves were analyzed using the linearized Poisson-Boltzmann equation with constant charge boundary [4.9-11] to determine the electrostatic interactions on the wool surface, Figure 4.3.

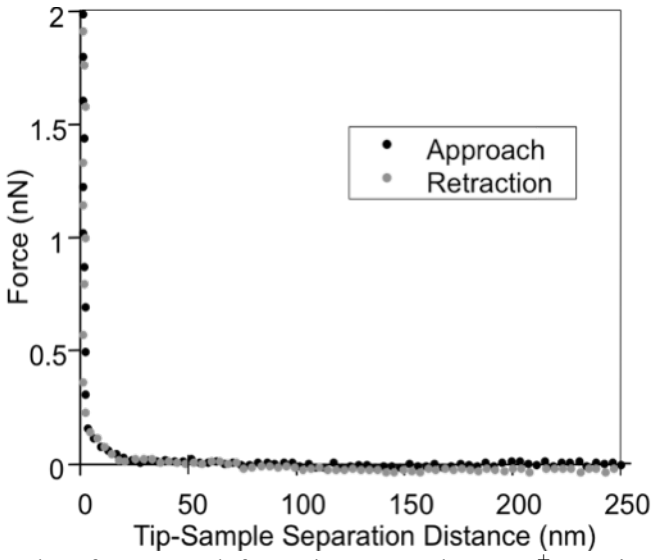

Figure 4.3: An example of a normal force between the NH_2^+ terminated SAM probe tip and wool fiber surface in a 0.0015M phosphate buffer solution, as a function of separation distance between the probe tip and fiber.

Using the linearized Poisson-Boltzmann theory, the electrostatic force, F, calculated between the hemispherical tip and the wool surface has the form [4.10-11]:

$$F = \frac{4\pi\sigma_{tip}\sigma_{wool}}{\varepsilon\,\kappa} e^{-\kappa D} \qquad 4.1$$

where s_{wool} is the charge density on the wool, s_{tip} is the charge density of the tip, ε is the permittivity of the fluid (6.923×10^{-10} C^2/Nm^2), κ^{-1} is the Debye length, and D is the tip-sample separation distance. From previous experiments on self-assembled monolayer coated control substrates, the surface charge densities of the carboxyl-terminated and amino-terminated tips were estimated to be -0.01 C/m^2 and +0.02 C/m^2 respectively [4.10-11]. The Debye length at 0.0015M NaCl; therefore, force-distance curves were fit for distances between 8 nm and 40 nm to minimize any short range non-electrostatic components of the interaction (including van der Waals forces) [4.17-19].

The charge interaction between the tip and sample is most clearly defined with the analysis of the force curves of like charges. A detection of negatively charged functional groups was possible by analyzing the approach curves of a charge map produced with a carboxylated probe. Likewise, detection of positively charged functional groups is possible with the analysis of approach curves of charge plots of an amino terminated probe. The adhesion corresponding to DTT functionalized probe force curves were indicative of disulfide bonding between the thiol of the DTT and a thiol of cysteine.

The application of the Poisson-Boltzmann equation does stretch the assumptions of the linearized model due to the low ionic strengths and small size of the tip [4.12]. However, since the goal of this study was to understand the trends in the distribution of charge over the surface of the fibers rather than the exact magnitude, the linearized PB

equation was used to minimize computation time on the 24,000 individual force curves analyzed.

4.2.3 Effect of Elevated pH on Amino Acid Charges

Evaluation the effect of pH on surface forces was considered in order to further distinguish locations of specific amino acids. By altering pH to such a value that only one amino acid remains significantly protonated, it is possible to distinguish to contribution of that specific functional group. For this process, the pH was elevated to the third pKa of arginine, 12.48 [4.20], well above the pKas of the other amino acids.

The previously described surface charge measurements by force spectroscopy and analysis with the PB equation were repeated on five scale with a 11-Amino-1-undecanethiol functionalized probe, replacing the PBS with ~12.48 pH NaOH, with a Debye length of ~8 nm. Since measurements were taken near the pKa of arginine, it was necessary to double the magnitude of the force charges for comparison to the charge density pH 7, at which arginine is fully proteinated. The tip charge was calculated according to Equation 4.2:

$$\sigma_{tip(pH=12.4)} = \sigma_{tip(pH=7)} 10^{\frac{pH}{pKa}} \qquad 4.2$$

where the surface pKa of the SAM is equal to 5. [4.21].

4.2.4 Labeling of carboxyl and amine groups with gold nanoparticles

To confirm results of the AFM charge mapping, gold nanoparticles were functionalized to attach to either the carboxyl, amine, or sulfur groups on the wool fiber. These labeled fibers were then imaged by backscatter SEM.

James Chow, a collaborating Clemson University Bioengineering student, developed the nanoparticle functionalization procedure and applied the DTT and carboxylated nanoparticles. Gold nanoparticles (Sigma, 20nm diameter) were functionalized with carboxyl groups using 10mM 11-mercaptoundecanoic acid or amino groups using 10mM 11-Amino-1-undecanethiol. The carboxylated and amino-functionalized nanoparticles were then treated with 1-ethyl-3-(3-dimethylaminopropyl) carbodiimide (EDC) hydrochloride and N-hydroxysulfosuccinimide (sulfo-NHS) and allowed time to react on cleaned wool fibers. Carboxyl terminated particles were then bound to the negatively charged functional groups on the wool surface while, in separate samples, amine-terminated particles were bound to the positively charged functional groups on the wool surface.

To identify sulfur atoms, a 100mM dithiolthreitol (DTT) solution was prepared. The DTT mixture was poured over wool and allowed to incubate for 2 hours at 37ºC. A gold nanoparticle solution was then poured over the wool samples and stored at cool temperature.

All treated wool fibers were dried, sputter coated with a thin coating of platinum (approximately 4 Å), and placed in a Hitachi S4800 Ultra High Resolution Field Emission SEM for backscatter electron (BSE) imaging. Due to the high atomic number of gold, relative to the background wool composition, the gold nanoparticles are easily identified, as they appear much brighter than their surroundings when viewed with the backscatter detector.

4.3 Results and Discussion

Topography of fiber scales was measured by contact mode AFM and showed that wool scales had curved ridges. The scales were fairly consistent in their morphology; they were found to be 565 +/- 124 nm in height and about 20mm long.

The surface charge of the wool fiber calculated using the NH_2^+ functionalized tip measuring the repulsion, Figure 4.4. The data were compiled to show the placement of positive-charged moieties on the fiber surface as a function of the fiber topography. Within 3μm of the scale edge, the average surface charge density due to the amine groups was estimated to be 0.0055 +/- 0.0012 C/m^2, Figure 4.4. Although there is variation in the measured surface charge density, clear trends were observed. As shown in Figure 4.5 for a sample scale, there were more positive charge groups with 0.5 micron on either side of the edge of the scale than further away.

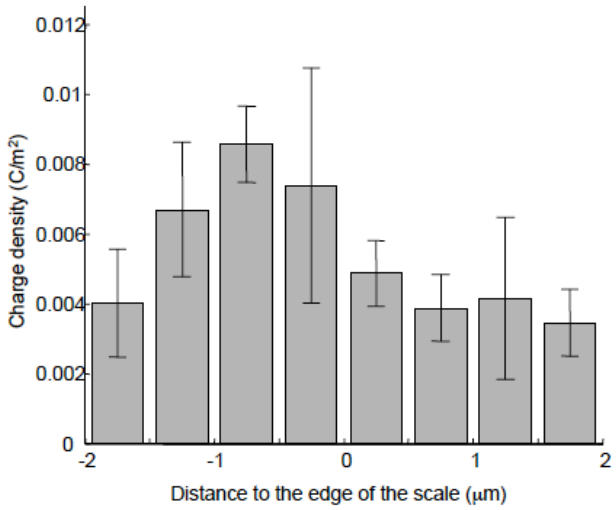

Figure 4.4: The average of surface charge per unit area from the HRFS data on five different scales using NH_2^+ SAM. The distance from the scale edge is normalized so that 0 is the middle of scale ridge.

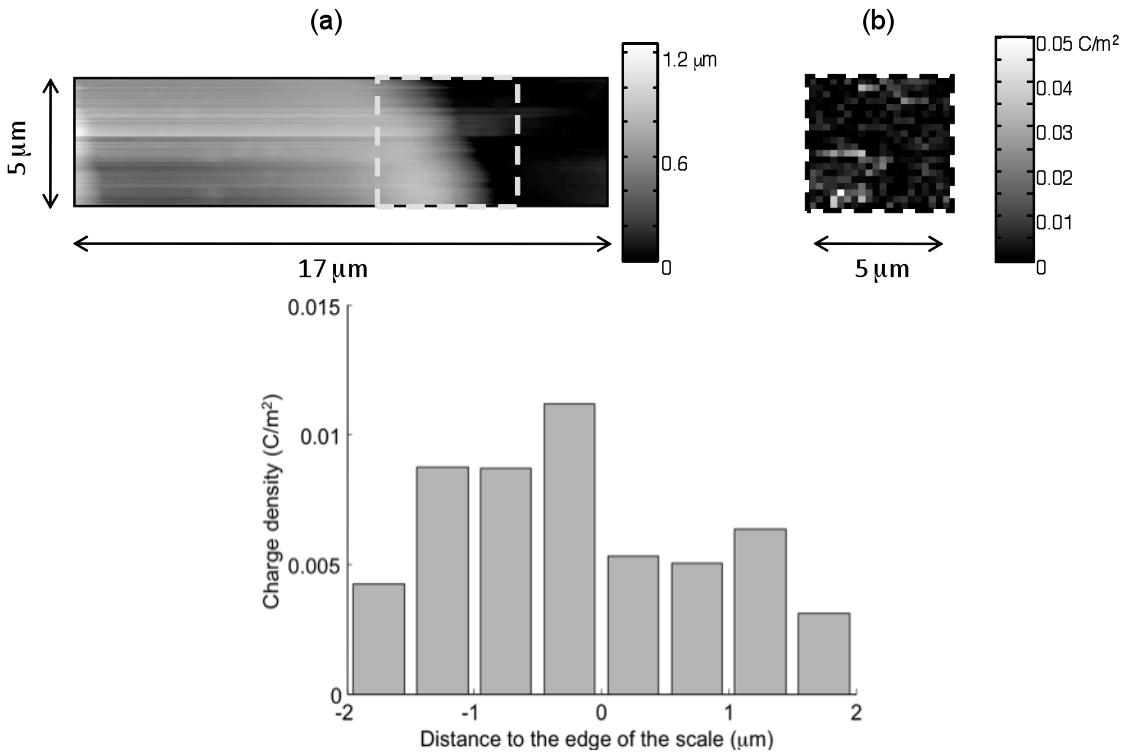

Figure 4.5: A contact mode AFM height image of a single representative merino wool fiber scale (A). The overlaid square shows the specific location probed with high-resolution force spectroscopy (HRFS). The corresponding charge map calculated from the HRFS data measured with the positively charged probe tip (B). Averaged surface charge density as a function of distance to the edge of the scale calculated from the charge map for a single scale. The distance from the scale edge was calculated so that the mid-point of the scale ridge was taken as 0. Positive charge areas are located closer to the edge of the scale (C).

There is an apparent trend in the averaged positive charge data over all scales (Figure 4.4); although the standard deviation is large due to variance between fibers, the average charge due to positive groups at distances greater than 2 microns from the edge of the scale was significantly lower than that within 1 micron from the edge ($p = 0.019$, paired t-test). This indicates that there is a high concentration of either lysine or arginine near the scale edge. This non-uniform distribution of primary amine groups (lysine and arginine) near the scale edge was further confirmed by the SEM images of nanoparticle functionalized wool fibers. As shown in Figure 4.6, the backscatter SEM revealed that although some nanoparticles were attached in the middle of the scales, the nanoparticles were predominantly found near scale edges.

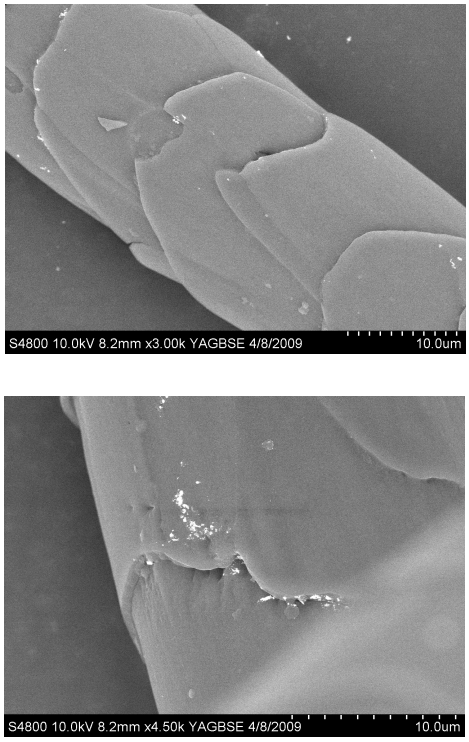

Figure 4.6: Backscatter SEM images of wool fibers with gold nanoparticles bound to Lysine and Arginine residues (A). Particles were found near scale edges (B).

The estimated negative surface charge measured from the COO^- functionalized tip force curves, Figure 4.7, indicates where there are negative charge moieties distributed somewhat evenly on the fiber surface. It also shows that these are not located preferentially along the scale ridge, Figure 4.8. This would indicate an evenly spaced distribution of aspartic or glutamic acids along the surface. In addition, the average surface charge density due to negative charged groups was -0.011 +/- 0.0059 C/m^2. This uniform distribution of acidic carboxyl groups was further confirmed by the backscatter

EM images of the gold labeled wool. As shown in Figure 4.9, the gold particles functionalized to attach to the carboxyl groups clusters were uniformly distributed over the wool fibers. In addition, the density of particles is higher in these images (Figure 4.8) than the images of the particles bound to amine residues. This further confirms that the net surface charge is negative.

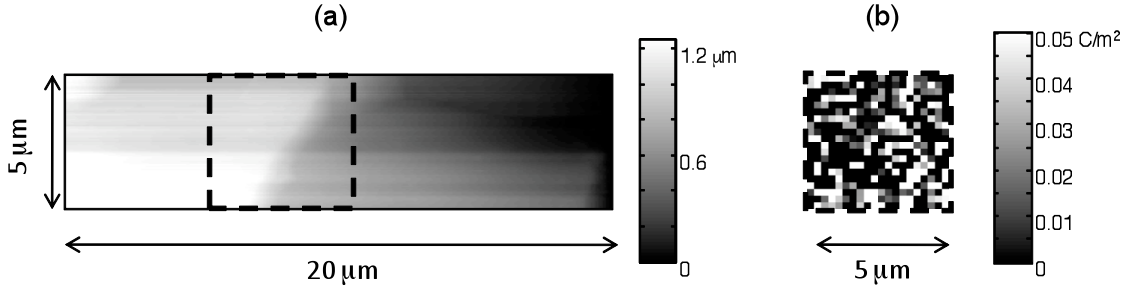

Figure 4.7: A contact mode AFM height image of a merino wool fiber scale (A). The overlaid square shows the specific location probed with high-resolution force spectroscopy (HRFS). The absolute value of the corresponding charge map calculated from the HRFS data measured with the negatively charged probe tip (B). This shows a random uniform distribution of negative charged areas over the surface of the scale edge.

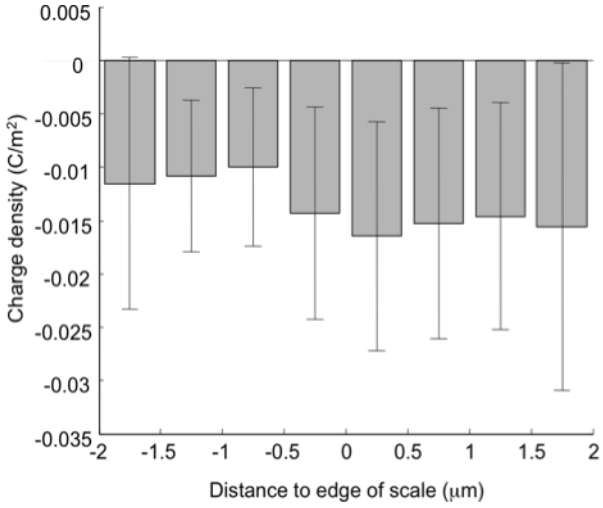

Figure 4.8: An approximation of the magnitude of the surface charge per unit area from the HRFS data across five scales using COO^- SAM. The distance from the scale edge is normalized so that 0 is the middle of the scale ridge. This shows an even distribution of acidic amino acid groups across the wool fiber surface.

A 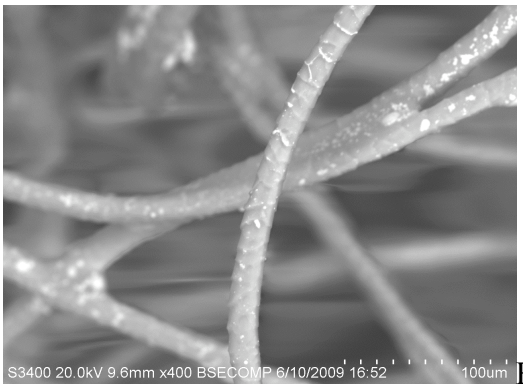

B 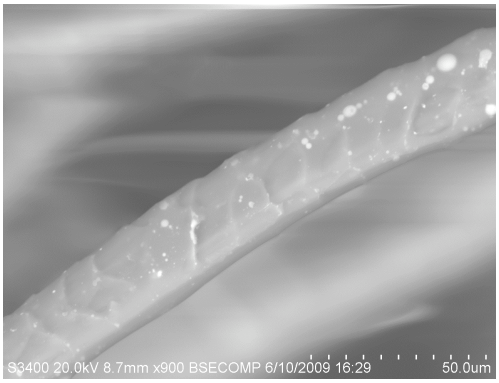

Figure 4.9: Backscatter SEM images of wool fibers with gold nanoparticles bound to glutamic acid and aspartic acid residues (A and B).

Adhesion maps corresponding to DTT functionalized AFM probes provide no indication of a correlation between disulfide interactions and proximity to scale edges or other distinguishable topographical feature, Figure 4.10. Furthermore, clusters of DTT functionalized nanoparticles are randomly distributed and non-uniform, Figure 4.11.

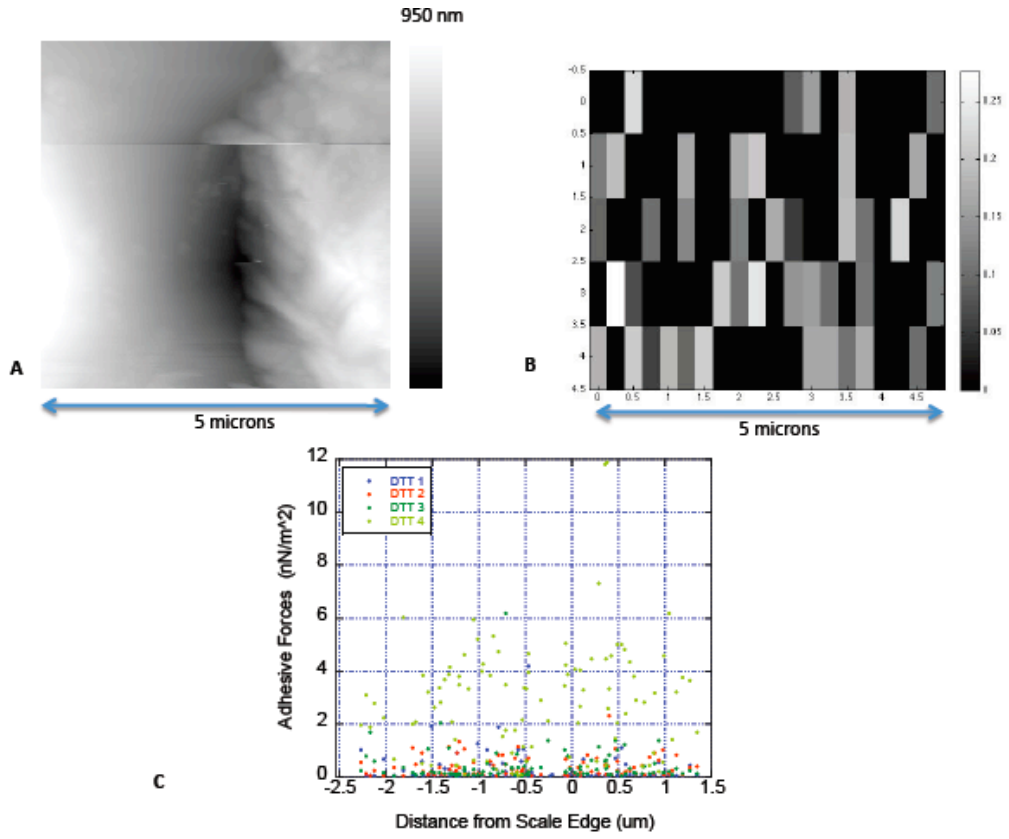

4.10: A topography image (A) and corresponding adhesion map (B) and plot of adhesion versus distance from the scale edge (C) measured with a DTT functinonalized AFM probe, showing uniform distribution of sulfur groups on the surface.

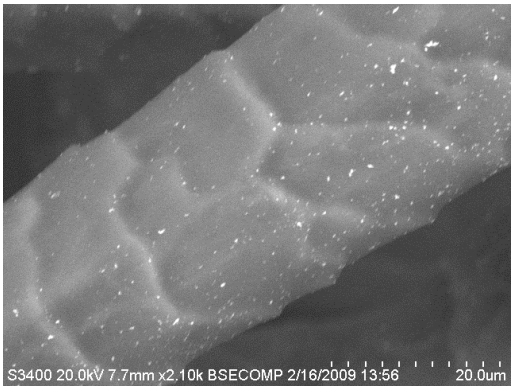

4.11: Backscatter SEM images of wool fibers with gold nanoparticles forming disulfide bonds to cysteine.

The average net surface charge density over a scale was found to be about -0.006C/m^2. Zeta potential, ζ, can be estimated from a charge density using the linearized Poisson-Boltzmann formation. Briefly, ζ is the potential at the slip plane, which is approximately the potential one Debye length, κ^{-1}, away from the surface. Since the potential decays exponentially away from the surface in the linear Poisson-Boltzmann formulation, the relationship between the surface charge density and the zeta potential is as previously described in Equation 4.1. Thus, a net average charge density over the surface of the wool fiber, -0.0055 C/m^2, will translate to a measured zeta potential of -23 mV, which is consistent with the previously published results on zeta potentials of -24 mV [4.9].

Force mapping at an elevated pH resulted in a slight loss of surface charge, Figure 4.12, due to the deproteination of lysine and partial deproteination of arginine. However, there is a large reduction in the charge density just below the scale edge.

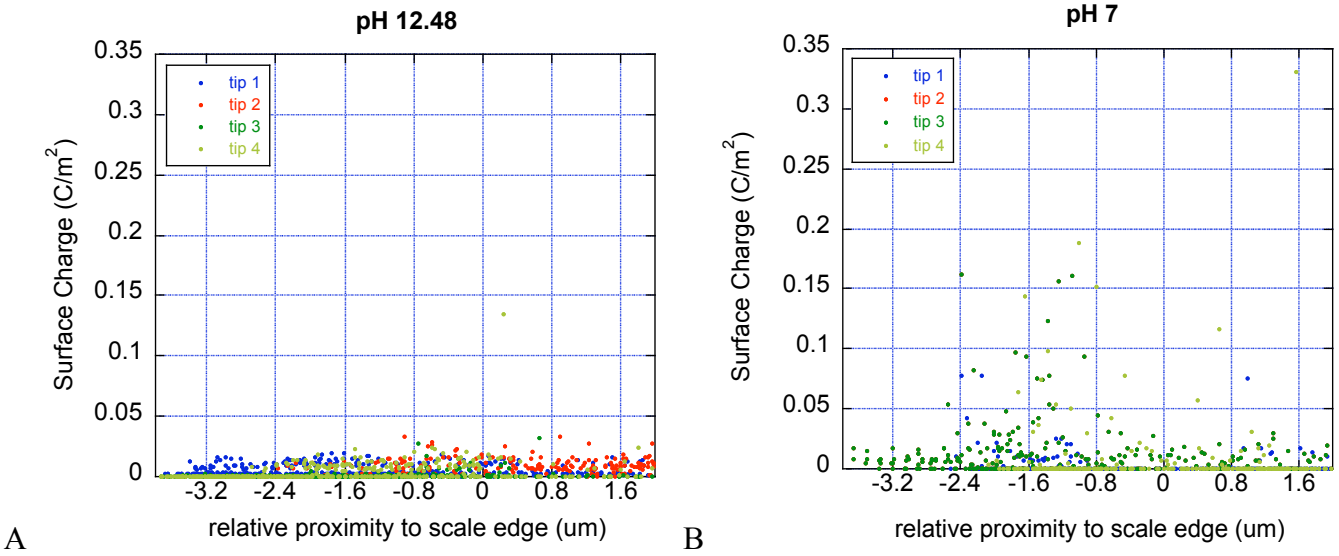

Figure 4.12: A plot of surface charge density versus distance from scale edge at pH 12.5 (A) and pH 7 (B).

4.4 Conclusion

This study determined charge density using high-resolution force spectroscopy, which has previously demonstrated adequate force sensitivity in an electrolytic fluid to permit the measurement of electrostatic interactions between the tip and the sample [4.10]. AFM was used to identifying trends in charge affiliated with the scales on the surface of wool so that amino acids could be mapped. Using only a standard probe in a salt solution, the fiber surface shows different charge with varying location, which presumably correlates with different chemical composition.

Mapping of specific charge groups using carboxyl (COO^-), amino (NH_2^+), and sulfur (DTT) functional groups indicate that although all scales have a net negative surface charge, there is variability between groups and certain scales seem to have more negatively charged groups on their surface than others. Negative charges seem uniformly distributed over the scale surface. The surface charge density is relatively high; on the

same order of magnitude as some self assembled monolayers [4.22]. This result likely correlates to a distribution of acidic amino acid residues. Since acidic, these AA residues can be only aspartic acid or glutamic acid. From the surface charge density measurements, the approximate density of acidic residues was estimated to be about 1 group per 15 nm^2 over the surface of the wool fiber.

However, as observed in both the AFM and SEM data, the surface of the wool is not homogeneous in the density of acidic groups. Although there was no prevalence for acidic groups at the edge of the scales or other topographical feature the fibers, the acidic groups were always found in small clusters as seen in the AFM charge maps and in the clustering of nanoparticles in the SEM images. Mapping did reveal the presence of positively charged domains near the scale edges. This result would indicate a localized concentration of basic amino acids.

When lysine is largely deprotonated at pH 12.5, only a slight reduction in charge density was observed, indicating that the primary constituent of wool scales is arginine, which is in agreement with previously published Raman Spectroscopy analysis of wool scale composition [4.8]. There is however a significant loss of charge just below the scale edge, indicating that perhaps lysine is the larger constituent at the base of the scale.

DTT functionalized AFM probes were analyzed to yield adhesion maps, which show random binding of the tip to the wool surface. There is no correlation between thiol groups and proximity to scale edges. Furthermore, DTT functionalized nanoparticles are randomly distributed and non-uniform. This binding pattern is consistent with the prediction that thiol groups are randomly distributed along the surface of wool fibers.

Overall, the density of groups resulted in a net average negative charge over the surface of the fiber. These results are consistent with previous measurements of wool zeta potentials, which concluded that wool was more negatively charged. AFM and backscatter SEM results are in agreement that clusters of carboxyl acid groups and cysteine groups are uniformly distributed over the surface of wool fibers while amine groups, namely lysine, are concentrated near the edge of scales.

August 27, 2009: "Alteration of Dentin-Enamel Mechanical Properties Due to Common Dental Whitening and Etching Treatments" submitted for consideration for publication in Journal of the Mechanical Behavior of Biomedical Materials.

CHAPTER FIVE

SUMMARY

This thesis characterizes the mechanical and chemical response of biological composite systems. Mechanical properties and chemical composition of human teeth were characterized by means of nanoindentation, FTIR and fluorescence microscopy. Chemical characterization of Merino wool fibers was done by high-resolution force spectroscopy. A better understanding of mechanical and chemical properties of naturally occurring systems will allow for prediction of bioresponse and optimize the engineering of synthetic biomaterials.

Analysis of the mechanical properties of dentin and enamel with the Oliver-Pharr model indicated changes resulting from common dental treatments and preparation for restorative procedures. These changes are associated with alterations in chemical composition and structure.

The surface chemistry of Merino wool fibers was analyzed to clarify the distribution of amino acids along the surface of wool fibers. Atomic force spectroscopy was used to detect positively charged, negatively charged, and sulfur functional groups on the surface and their relative proximity to surface features. SEM was used to verify AFM results by monitoring the binding locations of functionalized nanoparticles on wool surfaces.

APPENDICES

APPENDIX A

SENSITIVITY OF CELLS TO SUBSTRATE TOPOGRPAHY FOR APPLICATION TO CRANIAL RECONSTRUCTION

A.1 Introduction

Manipulating the surface topography of a biomedical device may induce atypical cell behavior, particularly in circumstances of long-term implantation [A.1]. The application of current analytical techniques, force spectroscopy and nanoindentation, in studies of ambiguous biological samples allow for the characterization of the cell response to mechanical and topographical traits of various surfaces. The investigation of dental pulp cells is unique and potentially revolutionary to the field of cranial reconstructive surgery.

Background

It is critical for the development of an accurate model of cell development and guidance, to determine cell preference and the effect substrate surface topography on biological response. Recent studies of stem cells bone marrow cells have demonstrated that surface structure control cell binding [A.2-4] as well as manipulate the large-scale cell adhesion and proliferation in vivo [A.5]. Compliance, chemistry, temperature, and roughness of substrate are among other surface properties factors that direct the bioresponse of the cells, as illustrated in Figure A.1 [A.3].

This project is unique in the use of dental pulp cells, which are potentially applicable for cranial reconstruction. Dental pulp cells are naturally arranged in a hexagonal array of tubules [B.14]. Perhaps, direction of cells to adhere and replicate in such a fashion could profoundly advance dental restoration practices. With the conclusion

of this study, observations of trends in cell behavior may be applied to development of a model that will more accurately predict dental pulp cell position and response as a function of the substrate topographical structure.

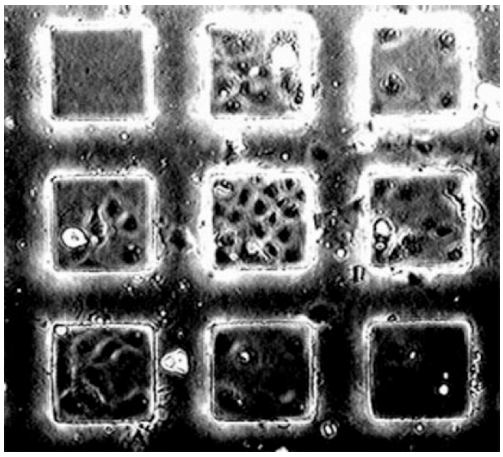

Figure A.1: A series of substrates with patterned regions of various moduli. Adherent cos-7 cells were cultured, in Gray fashion, on substrates with periodic patterns of varying stiffness, while the chemical environment was unchanged. Cells preferred growth on stiffer regions [A.3].

Though no attention has been given to the response of dental pulp cells to substrate properties, based on previously reported behavior of other types of cells, it is anticipated that dental pulp cells will preferentially adhere to specific surfaces. Cell proliferation will depend on the mechanical properties and surface characteristics of the substrate. The development of an accurate model to predict cell response, as a function of the substrate surface topography, will have biomedical benefits. Manipulating substrate surfaces may allow for the development of implant materials for cranial reconstruction, which manipulate cell adhesion and expedite the healing process.

Objective of the Problem- Hypothesis

This study will clarify the influence of surface structure found in thin film sensors used for biomedical applications [A.6-7]. The hypothesis of concern is that substrate topography could be used to manipulate dental pulp cell response. The sensitivity and preference of a cell can be evaluated by common surface sensing techniques.

Topographical structures frequently investigated in previous studies of other cell types [A.8] include holes [A.9] continuous [A.10-12] and discontinuous grooves [A.13] of varying sizes. The aforementioned substrate designs, as well as novel designs, specifically honeycombs of various dimensions, will be investigated.

4.2 Possible Experimental Plan

This work involves the characterization of different silica substrates according to their surface roughness. The first goal of this project is to use photolithography to construct a variety of specific surfaces on substrates. A uniform gold coating will then be applied to ensure consistent surface chemistry, thus allowing for isolation of the effect of topography. Cells will then be deposited onto these substrates and monitored by SEM, AFM, and time-lapse contrast and fluorescent imaging. The background fluorescence of sputtered gold examined in preparation for this study, was found to be very low. Thus cell responses are expected to be readily identifiable. This work will allow for the determination of cell sensitivity and cells' preferred surface structure and design of surfaces to initiate growth of certain cells and control cell migration and encourage selective cell proliferation.

Substrate Preparation	Micro-construction of substrate surfaces will be accomplished primarily of photolithography, Figure A.2. Manufactured structures will include trough-like grooves, discontinuous grooves, holes, and hexagonal honeycomb structures of various diameters, as represented in Figure A.3. To isolate the effects of topography and ensure uniform surface chemistry, a~ 10nm gold coating will be applied.
Substrate Characterization	Characterization and sensing surface topography will be possible with Atomic Force Microscopy (AFM) and Scanning Electron Microscopy (SEM)[A.14].
Cell Preparation	
Cell Deposition	
Observation of Cell Behavior	Monitoring of cell movement will also use AFM and SEM, as well as time-lapse phase contrast and fluorescent imaging of cell cultures [A.3].

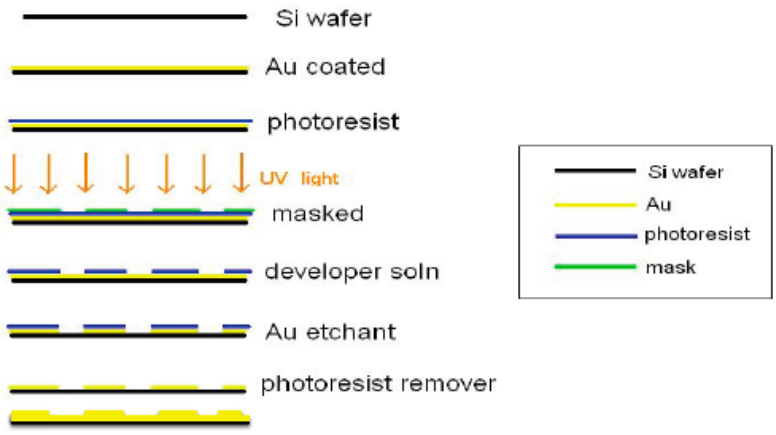

Figure A.2: An illustration of the general photolithography procedure.

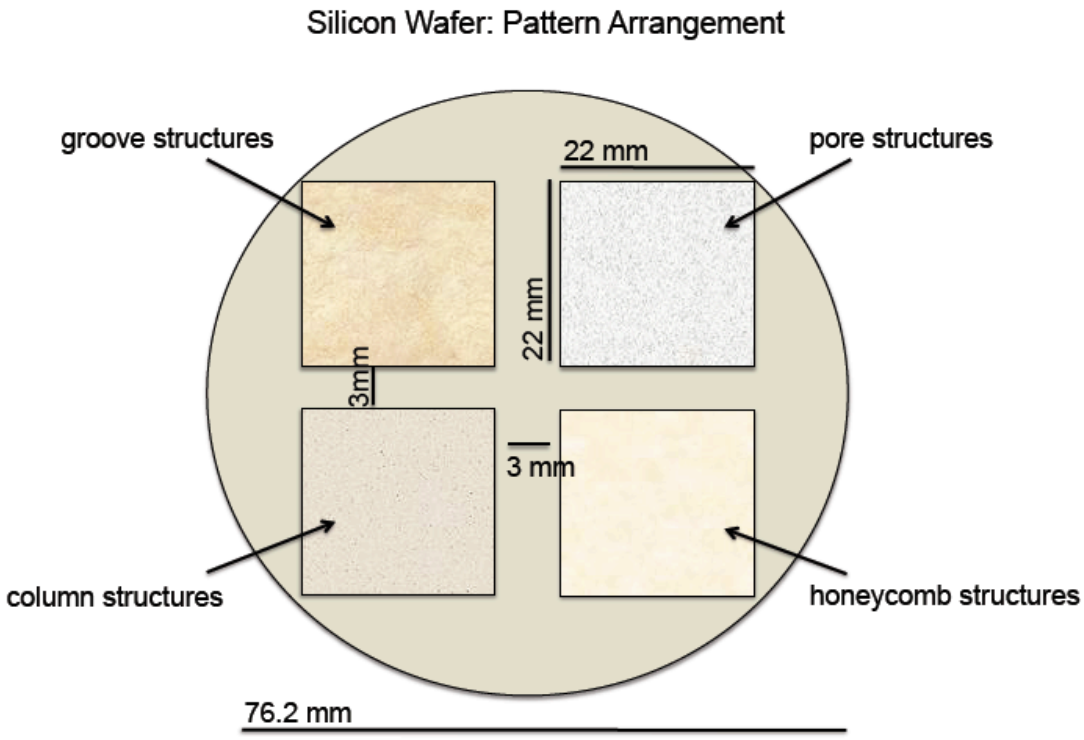

Figure A.3: A representative layout of a photolithography mask.

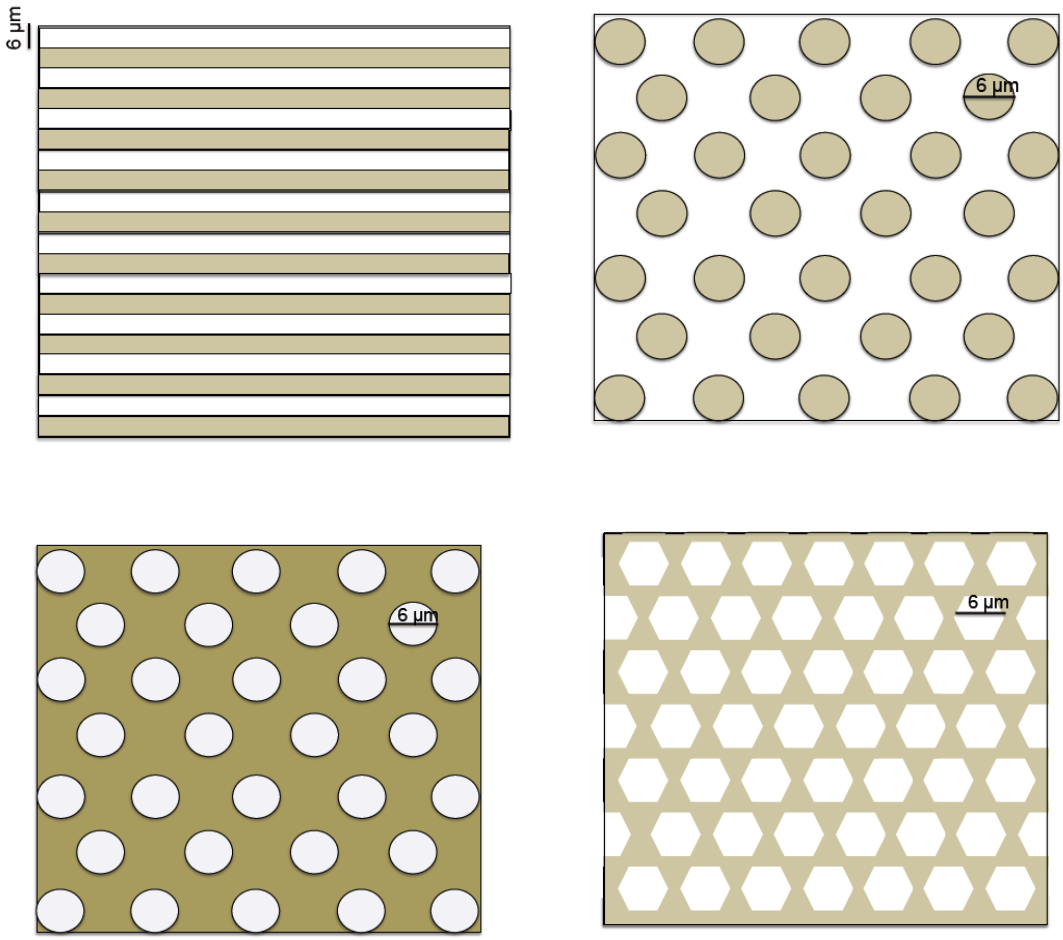

Figure A.4 Arrangement of feature on the photolithography mask. The features shown represent for 6um diameters. Masks will also be constructed with features of 12µm, 25µm, and 50µm diameters.

APPENDIX B

ADDITIONAL SEM IMAGES OF ENAMEL

SEM was used to view untreated teeth and treated teeth at various magnifications in order to gather additional images regarding the tooth surface with regards to microscopic morphological change associated with treatment conditions.

A

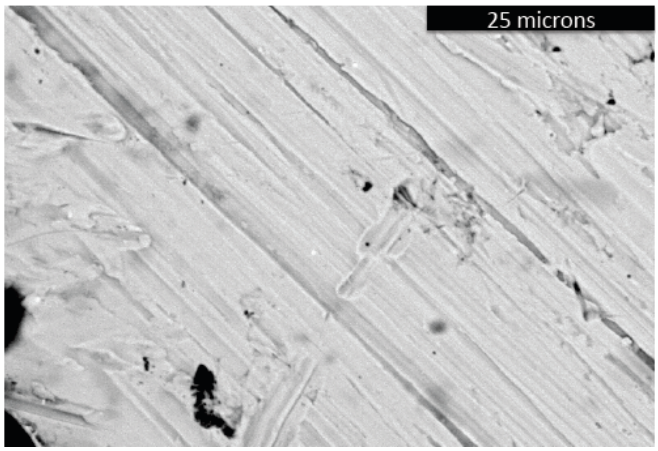

B

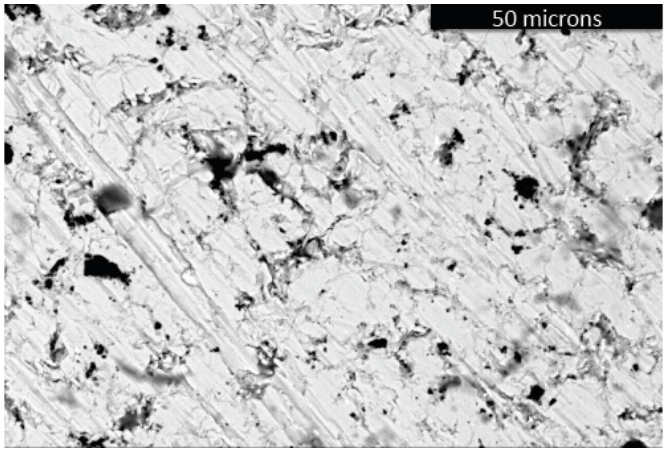

Figure B.1: SEM images of UltraEtch ™ treated tooth of enamel (A) and dentin (B)

REFERENCES

CHAPTER 1

1.1 Chim H, Gosian AK. Biomaterials in Craniofacial Surgery: Experimental Studies and Clinical Application. J of Craniofac Sur. 20, 1 [2009] 29-33.

1.2 Callister WD Jr. "Fundamentals of Materials Science and Engineering". 2nd Ed. John Wiley & Sons, Inc. Salt Lake City, UT 2005.

1.3 Meredith JC. Combinatorial characterization of cell interactions with polymer surfaces. J Biomed Mater Res 66A, 3 [2003] 483-490.

1.4 Tziampazis E, Prabhas JK, Moghe V. PEG-variant biomaterials as selectively adhesive protein templates: model surfaces for controlled cell adhesion and migration. Biomaterials. 21 [2000] 511-520.

1.5 Sarikaya, M, Molecular biomimetics: nanotechnology through biology. Nat Mater. 2, 9 [2003] 577-585.

1.6 Jung LS, Campbell CT, Chinowsky TM, Mar MN, Yee SS. Quantitative Interpretation of the Response of Surface Plasmon Sensors to Adsorbed Films. Lamgmuir. 14 [1998] 5636-5648.

1.7 Mrksich M. What Can Surface Chemistry do for Cell Biology. Chem Biol. 6 [2002] 794-797.

1.8 Chen X, Ferrigno R, Yang J, Whitesides GM. Redox Properties of Cytochrome c Adsorbed on Self-Assembled Monolayers: A Probe for Protein Conformation and Orientation. Langmuir. 18 [2002] 7009-7015.

1.9 Lim JY, Donahue HJ. Cell Sensing and Response to Micro- and Nanostructured

Surfaces Produced by Chemical and Topographic Patterning. Tissue Eng. 13, 8 [2006] 1879-1891.

1.10 Chen CS. Geometric control of cell life and death. Science.276, 5317 [1997] 1425-1428.

1.11 Kraft O. Size Effects on Deformation and Fatigue of Metallic Thin Films and Small: Structures: Experiments and Dislocation Dynamics Simulation. Mechanical Behaviour of Systems at Small Length Scales - 2 Diamond Jubilee Celebrations 2006-2007. [2007] 1200 – 1240.

1.12 Garcia A, Boettiger D, Modulation of cell proliferation and differentiation through substrate-dependent changes in fibronectin conformation. Mol Biol Cell. 10 [1999] 785-798.

1.13 Jones JR. Observing cell response to biomaterials. Royal Academy of Engineering/EPSRC Research Fellow. 9,12 [2006] 34-43.

1.14 Hole BB, Schwarz JA, Gilbert JL, Atkinson BL. A study of biologically active peptide sequences (P-15) on the surface of an ABM scaffold (PepGen P-15^{TM}) using AFM and FTIRJ. Biomed Mater Res. 74A, 4 [2005] 712.

1.15 Veiseh M, Zareie H, Zhang M. Highly Selective Protein Patterning on Gold−Silicon Substrates for Biosensor Applications. Langmuir. 18, 17 [2002] 6671–6678.

1.16 Zreiqat H, Valenzuela SM, Nissan BB, Roest R, Knabe C, Radlanski RJ, Renz H, and Evans PJ. The effect of surface chemistry modification of titanium alloy on signalling pathways in human osteoblasts. Biomaterials. 26, 36 [2005] 7579-7586.

1.17 Spargo BJ, Spatially controlled adhesion, spreading, and differentiation of endothelial cells on self-assembled molecular monolayer. Proc Nat Acad Sci. 91 [1994] 11070-11074.

1.18 Craighead HW, Turner SW, Davis RC, James C, Perez AM, St. John PM, Isaacson MS. Chemical and Topographical Surface Modification for Control of Central Nervous System Cell Adhesion. Curr Opinion in Sol St & Mater Sci. 5 [2001] 177-184.

1.19 Chanchaona S. Biomimicry. King Monkut's University of Technology Thonburi, Biological Engineering. http://www.bioeng.kmutt.ac.th/news/Biomimetic.pdf. Website Accessed 10/13/09.

1.20 Ritchie R, Muhlstein C, Nalla R. Failure by fracture and fatigue in "nano" and "bio" materials. JSME International Journal, Series A. 47, 3 [2004] 238-251.

1.21 Riggs BL, Melton LJ III, O'Fallon WM. Drug therapy for vertebral fractures in osteoporosis: evidence that decreases in bone turnover and increases in bone mass both determine antifracture efficacy. Bone. 18, 3 [1996] 197S–201S.

1.22 Christou A. Materials and reliability issues in MEMS and Microsystems. Materials Science and Engineering. University of Maryland. http://www.mse.umd.edu/faculty/faculty_profiles/christou/MEMSspieAUSTR.pdf. Website Accessed 10/01/09.

1.23 Hairul Nizam B, Lim C, Chang H, Yap A.J. Nanoindentation study of human premolars subjected to bleaching agent. J Biomech. 38, 11 [2005] 2204-

2211.

1.24 Church J. The Analysis of Merino Wool Cuticle and Cortical Cells by Fourier Transform Raman Spectroscopy; Wiley Periodicals, Inc. 42, 1 [2008] 7-17.

1.25 Huang S, Shape-dependent control of cell growth, differentiation, and apoptosis: Switching between attactors in cell regulatory network. Exp Cell Res. 261 [2000] 91-103.

REFERENCES

Chapter 2

2.1 Holland NB, Marchant RE, Individual plasma proteins detected on rough biomaterials by phase imaging AFM. J. Biomed. Mater. Res. Part A. 51, 3 [2000] 307-315.

2.2 Bovi M, Gassler N, Hermanns-Sachweh B. Determination of the biocompatibility of biomaterials by scanning electron microscopy (SEM). EMC 2008 14th European Microscopy Congress 1–5. Springer Berlin Heidelberg. Aachen, Germany. 2008.

2.3 Dickinson ME, Wolf KV, Mann AB. Nanomechanical and chemical characterization of incipient in vitro carious lesions in human dental enamel. Arch of Oral Bio. 52, 8 [2007] 753-760.

2.4 Callister WD Jr. "Fundamentals of Materials Science and Engineering". 2nd Ed. John Wiley & Sons, Inc. Salt Lake City, UT 2005.

2.5 Ebenstein DM, Pruitt LA. Nanoindentation of biological materials. Nanotoday. 1, 3 [2006] 26-33.

2.6 Oliver WC, Pharr GM. An improved technique for determining hardness and elastic modulus using load and displacement sensing indentation experiments. J Mater Res., 7 [1992] 1564-1583.

2.7 Fischer-Cripps AC. "Nanoindentation" 2nd Ed. Mechanical Engineering Series. Springer. NY, NY 2004.

2.8 Cornell University. Nanoindentation. http://www.nanoindentation.cornell .edu/home_main.html. Website Accessed 06/01/09.

2.9 Simmons G, Wang H. “Single Crystal Elastic Constants and Calculated Aggregate Properties: A Handbook” MIT Press. Cambridge, MA, 1971.

2.10 Oliver W, Pharr G. Review: Measurement of hardness and elastic modulus by instrumented indentation: Advances in understanding and refinements to methodology. Mater Resear Soc. 19, 1 [2004] 3-20.

2.11 Tyagi P, Catledge SA, Stanishevsky A, Thomas V, Vohra YK. Nanomechanical Properties of Electrospun Composite Scaffolds Based on Polycaprolactone and Hydroxyapatite. Nanosci Nanotechnol. 9 [2009] 4839.

2.12 Navamathavan R, Moon Y, Kim G. Lee TG, Hahn J. Park S. ‘Pop-in’ phenomenon during nanoindentation in epitaxial GaN thin films on c-plane sapphire substrates. Mater Chem Phys. 99, 2-3 [2006] 410-413.

2.13 Tang B, Ngan AHW. Accurate measurement of tip-sample contact size during nanoindentation of viscoelastic materials J Mater Res. 18 [2003] 1141-1148.

2.14 Feng G, Ngan AHW. Effects of creep and thermal drift on modulus measurement using depth-sensing indentation. J Mater Res. 17 [2002] 660-668.

2.15 Ngan AHW. Wang HT, Tang B, Sze KY. Correcting power-law viscoelastic effects in elastic modulus measurement using depth-sensing indentation. Int. J Solids Struct. 42, 5-6 [2005] 1831-1846.

2.16 Cheng YT, Ni W, Cheng C. Determining the instantaneous modulus of viscoelastic solids using instrumented indentation measurements. J Mater Res. 20 [2005] 3061-3071.

2.17 Bembey AK, Oyen ML, Bushby AJ, and Boyde A. Effect of Water on Mechanical Properties of Mineralized Tissue Composites. Philos Mag. 86 [2006] 5691- 5703.

2.18 Balooch M, Wu-Magidi IC, Balazs A, Lundkvist AS, Marshall SJ, Marshall GW, Siekhaus WJ, Kinney HJ. Viscoelastic properties of demineralized human dentin measured in water with atomic force microscope (AFM)-based indentation. J Biomed Mater Res. 40 [1998] 539-544.

2.19 Rho JY, Zioupos P, Currey JD, Pharr GM, Variations in the individual thick lamellar properties within osteons by nanoindentation. Bone. 25, 3 [1999] 295-300.

2.20 Habelitz S, Marshall SJ, Marshall GW Jr, Balooch M. Mechanical properties of human dental enamel on the nanometre scale Arch Oral Biol. 46, 2 [2001] 173-183.

2.21 Carrillo F, Gupta S, Balooch M, Marshall SJ, Marshall GW, Pruitt L, Puttlitz C. Nanoindentation of polydimethylsiloxand elastomers: Effect of crosslinking, work of adhesion and fluid environment on elastic modulus. J Mater Res. 20 [2005] 2820-2830.

2.22 Grunlan JC, Xia A, Rowenhorst D, Gerberich WW. Preparation and evaluation of tungsten tips relative to diamond for nanoindentation of soft materials. Rev Sci Instrum. 72 [2001] 2804-2810.

2.23 Weaver JMR, Wickramasinghe HK. Semiconductor characterization by scanning force microscope surface photovoltage microscopy. J Vac Sci Tech B. 9, 3 [1991] 1562-5

2.24 Meyer E, Howald L, Overney R, Brodbeck D, Luthi R, Haefke H, Fromer J, Guntherodt HJ. Structure and dynamics of solid surfaces observed by atomic force microscopy. Ultramicroscopy. 42-44, A [1992] 274-80.

2.25 Kado H, Yokoyama K, Tohda T. A novel ZnO whisker tip for atomic force microscopy. Ultramicroscopy, 42-44, B [1992] 1659-1663.

2.26 Uppsala Universitet Pharmaceutical Physical Chemistry; Instrumentation: AMF Website Accessed 06/08/09.

2.27 Tranchida D, Piccarolo S. Local Mechanical Properties by Atomic Force Microscopy Nanoindentations. Applied Scanning Probe Methods XI, NanoScience and Technology. Springer Berlin Heidelberg, 2009.

2.28 Camensano TA, Logan BE. Probing bacterial electrosteric interactions using atomic force microscopy. Environ Sci Technol. 34, 16 [2000] 3354-3362.

2.29 Johnson AS, Hehl CL, Mason MG, Hafner JH. Fluid Electric Force Microscopy for Charge Density Mapping in Biological Systems. Langmuir. 19 [2003] 10007-10010.

2.30 Alonso JL, Goldmann WH. Feeling the Forces: Atomic force Microscopy in cell biology. Life Sci. 72, 23 [2003] 2553-2560.

2.31 Lebedev DV, Chuklanov AP, Bukharaev AA, Druzhinina OS. Measuring Young's modulus of biological objects in a liquid medium using an atomic force microscope with a special probe. Tech Phys Lett. 35, 4 [2009] 371-374.

2.32 Gibson CT, Watson GS, Mapledoram LD, Kondo H, Myhra S. Characterisation of organic thin films by atomic force microscopy—application of force vs.

distance analysis and other modes. Appl Surf Sci. 144-145 [1999] 618-622.

2.33 Goodhew PJ, Humphreys J, Beanland R. "Electron Microscopy and Analysis". 3rd Edition. Taylor and Francis. London. 2001.

2.34 Iowa State University "Welcome to the World of Scanning Electron Microscopy" Materials Science and Engineering Department. http://mse.iastate.edu/microscopy/prep.html. Website Accessed 6/14/09.

2.35 Sokolva T, Surmenka E, Tuchin V, Kishen A, Chebotarevsky A, Yu V. Spectroscopic study of demineralization and restoration processes in dental enamel. Progress in Biomedical Optics and Imaging - Proceedings of SPIE, Diagnostic Optical Spectroscopy in Biomedicine IV 6628. 2007.

2.36 Syddansk Universitet: Science in Your Eyes: Scanning Electron Microscope. http://scienceinyoureyes.memphys.sdu.dk/Sem_en.php. Website Accessed 06/08/09.

2.37 Robinson V N E. A wet stage modification to a scanning electron microscope. J Microsc. 103 [1975] 71-77.

2.38 Robinson V N E. The SEM examination of wet specimens. Scanning. 1 [1978] 149-156.

2.39 Kuboki K. Development of a variable pressure scanning electron microscope. Hitachi Instrument News. 25 [1993] 24-29.

2.40 Kuboki K, Wada M. Scanning electron microscopy of food items using a variable-pressure SEM. Hitachi Rev. 45 [1996] 31-34.

2.41 CalTech. Introduction to Fourier Transform Infrared Spectrometry. Thermo

Nicolet Corporation. 2001.

2.42 Sheffield Hallam University Materials and Engineering Research Institute. "FTIR spectroscopy" Equipment and specialist techniques. http://www.shu.ac.uk/research/meri/equipment/spectroscopy.html Website Accessed 6/14/09.

2.43 The Beckman Institute at the University of Illinois. The Image Technology Group. Fluorescence Microscopy. http://www.itg.uiuc.edu/publications/techreports/99-006/fluorescence.htm Website Accessed. 6/20/09.

2.44 Rice G, Fluorescent Microscopy. Microbial Life: Education Resources. Montana State University. Website Accessed 6/04/09.

2.45 Hirvonen L, Wicker K, Mandula O, Heintzmann R. Structured Illumination Microscopy of a Living Cell. J Eur B Eur Biophys. 38 [2009] 807–812.

REFERENCES

Chapter 3

3.1 Marshall G, Balooch M, Gallagher R, Gansky S, Marshall S. Mechanical Properties of the dentinoenamel junction: AFM studies of nanohardness, elastic modulus, and fracture. J Biomed Mater Res [2001] 87 – 95.

3.2 Fong, M. Sarikaya, S. N. White, M. L. Snead MRS. Nano-Mechanical Properties Across Dentin-Enamel Junction of Adult Human Incisor Teeth. Mat Sci Eng C—Bio, 7 [2000] 119–128.

3.3 Balooch M, Wu-Magidi IC, Lundkvist AS, Balazs A, Marshall SJ, Marshall GW, Seikhaus WJ, Kinney JH. "Viscolelastic Properties of Demineralized Human Dentin in Water with Atomic Force Microscopy (AFM)-Based Indentation", J Biomed Mater Res. 40 [1998] 539-544.

3.4 Hughes CE, White CA. Crack propagation in teeth: a comparison of perimortem and postmortem behavior of dental materials and crack. J Forensic Sci. 52, 2 [2009] 263-266.

3.5 Habelitz S, Marshall S, Marshall G Jr, Balooch M. Mechanical properties of human dental enamel on the nanometre scale. Arch Oral Biol [2001] 173-183.

3.6 Arends J, Stokroos I, Jongebloed WG, Ruben J. The diameter of dentinal tubules in human coronal dentine after demineralization and air drying. A combined light microscopy and SEM study. Caries Res. 29, 2 [1995] 118-121.

3.7 Lee J, Nettey-Marbell A, Cook A, Pimenta L, Leonard R, Ritter A. Using

Extracted Teeth for Research: The Effect of Storage Medium and Sterilization on Dentin Bond Strengths. J Am Dent Assoc. 138, 12 [2007] 1599-1603.

3.8 Hairul Nizam B, Lim C, Chang H, Yap A.J. Nanoindentation study of human premolars subjected to bleaching agent. J Biomech. 38, 11 [2005] 2204-2211.

3.9 Finke M, Hughes JA, Parker DM, Jandt KD. Mechanical properties of in situ demineralised human enamel measured by AFM nanoindentation. Surface Science. 491, 3 [2001] 456-467.

3.10 Willems G, Celis J, Lambrechts P, Braem M, Vanherle G. Hardness and Young's Modulus determined by nanoindentation technique of filler particles of dental restorative materials compared with human enamel. J Biomed Mater Res. 27 [1993] 747-755.

3.11 Habelitz S, Marshall G Jr, Balooch M, Marshall S. Nanoindentation and storage of teeth. J Biomech. 35 [2002] 995-998.

3.12 Park S, Wang D, Zhang D, Romberg E, Arola D. Mechanical properties of human enamel as a function of age and location in the tooth. J Mater Sci Mater Med. 19 [2008] 2317-2324.

3.13 Gustafson AG. A Morphologic Investigation of Certain Variations in the Structure and Mineralization of Human Dental Enamel, Odontol Tidskrift 67 [1959] 361-472.

3.14 Carolina Biological Supply Company. Caroplastic Embedding Sets. http://www.carolina.com/product/life+science/biological+displays/specime

ns+in+display+cases/caroplastic+embedding+set+2.do Website Accessed 7/20/08.

3.15 Ferguson VL, Boyde A, Bushby AJ. Elastic modulus of dental enamel: effect of enamel prism orientation and mineral content. Mater Res Soc Symp Proc. [2005] 841.

3.16 Abrahão I, Ivete J. Collagen analysis in human tooth germ papillae. Braz Dent J. 17 [2006] 208-212.

3.17 Palosaari H. Matrix metalloproteinases (MMPs) and their specific tissue inhibitors (TIMPs) in mature human odontoblasts and pulp tissue. J Dent Res. 81, 5 [2002] 354-359.

3.18 Fischer-Cripps AC. "Nanoindentation". 2nd ed. Spring-Verlang LLC, NY, NY 2004.

3.19 Garberoglio R, Brannstrom M. Scanning electron microscopic investigation of human dentinal tubules. Arch Oral Biol 16, 21 [1976] 355-362.

3.20 Angker L, Swain M, Kilpatrick N. Micro-mechanical characterization of the properties of primary tooth dentine. J Dent. 31 [2003] 261–267.

3.21 Zhou J, Xiao S, Lu X, Wang J, Weng J. A study on improving mechanical properties of porous HA tissue engineering scaffolds by hot isostatic pressing. Biomed Mater. [2006] 188–192.

3.22 Swift E Jr, Edwards G, Perdigão J, Thompsona J, Nunesa M, Ruddelld D, Negishi A. Free-electron laser etching of dental enamel. J Dent. 29 [2007] 347-353.

3.23 Fattibene P, Carosi A, De Coste V, Sacchetti A, Nuvara A, Postorino P, Dore P.

A Comparative EPR, infrared and Ramen Study of natural and deprotinated teeth enamel and dentin. P Phys Med Biol. 50 [2005] 1095-1108.

3.24 Xu H, Smith D, Jahanmir S, Romberg E, Kelly JR, Thompson V, Rekow E. Indentation damage and mechanical properties of human enamel and dentin. J Dent Res, 77, 33 [1998] 472-480.

3.25 Habelitz S., Marshall S Marshall G Jr, Balooch M. Mechanical Properties of Human Dental Enamel on the nanometer scale. Arch. Oral. Biol. 46 [2001] 173-183.

3.26 Mann A, Dickinson M, Monogr. The Teeth and Their Environment. Monogr Oral Sci. Basel, Karger, Oral. Sci. 19 [2006] 105-131.

3.27 Staines M., Robinson W, Hood J. Spherical indentation of tooth enamel. J of Mater Sci. 16 [1981] 2551-2556.

3.28 Balooch G, Marshall G, Marshall S, Warren O. Evaluation of a new modulus mapping technique to investigate microstructural features of human teeth. J Biomech. 37 [2004] 1223-1232.

3.29 Kinney J, Balooch M, Marshall S, Marshall G Jr, Weihs T. Atomic force microscope measurements of the hardness and elasticity of peritubular and intertubular human dentin. J Biomech Eng. 118, 1 [1996] 133-135.

3.30 Fong H, Sarikaya M, White S, Snead M. Materials Science & Engineering C, Biomimetic and Supramolecular Systems. [2000] 119-128.

3.31 Oliveira S, Pugach M, Hilton J. The influence of the dentin smear layer on adhesion: a self-etching primer vs. a total-etch system. Dent Mater. 19

[2003] 758-767.

3.32 Watari F. In situ quantitative analysis of etching process of human teeth by atomic force microscopy. J Electron Microsc. 54, 3 [2005] 299-308.

3.33 Fattibene P, Carosi A, De Coste V, Sacchetti A, Nuvara A, Postorino P, Dore P.A Comparative EPR, infrared and Raman Study of natural and deproteinated teeth enamel and dentin Phys Med Biol. 50 [2005] 1095-1108.

REFERENCES

Chapter 4

4.1 Min L, Yu L, Wei-yuan Z. Gray synthetic evaluation on moisture comfort of sportswear fabrics under the condition of heavy sweating. J of Donghua Univ. 4, 1 [2007] 146-50.

4.2 Parbhu AN, Bryson WG, Lal R. Disulfide Bonds in the Outer Layer of Keratin Fibers Confer Higher Mechanical Rigidity: Correlative Nano-Indentation and Elasticity Measurement with an AFM. Biochemistry. 38 [1999] 11755-11761.

4.3 Pille L. Adsorption of Amino-Functional Polymer Particles onto Keratin Fibres; Journal of Colloid and Interface Science. 198 [1998] 368-377.

4.4 Das T, Ramaswamy, G. N.; Enzyme Treatment of Wool and Specialty Hair Fibers. Textile Research Journal. 72, 2 [2006] 126-133.

4.5 Blackburn S. Products of the Hydrolysis of Wool Keratin by Papain. Nature. 165 [1950] 316 – 317.

4.6 Ryu J, Wakida T, Takagishi T. Effect of Corona Discharge on the Surface of Wool and Its Application to Printing; Textile Research Journal. 61, 10 [1991] 595-601.

4.7 Church J. The Analysis of Merino Wool Cuticle and Cortical Cells by Fourier Transform Raman Spectroscopy. Wiley Periodicals, Inc. 42, 1 [2008] 7-17.

4.8 Stewart K, Spedding PL, Otterburn MS, Lewis DM. Surface Layer of Wool. 1. Dityrosine Synthesis and Characterization. J Appl Polym Sci. [1997] 2359-2363.

4.9 Grancaric AM, Tarbuk A, Pusic T. Electrokeinetic properties of textile fabric. Coloration Technology. 22 [2005] 221–227.

4.10 Vandiver J, Dean D, Patel N, Bonfield W, Ortiz C, Nanoscale variation in surface charge by snthetic hydroxyapatite detected by chemically and spatially specific high-resolution force spectroscopy. Biomaterials. 26, 3 [2005] 271-283.

4.11 Dean D. Molecular Electromechanics: Modeling Electrostatic Forces Between Glycosaminoglycan Molecules. Masters Thesis. MIT Dept of EECS. May 2001.

4.12 Carr C, Leaver I, Hughes A, X-Ray Photoelectron Spectroscopic Study of the Wool Fiber Surface; Textile Research Journal. 56, 7 [1986] 457-61.

4.13 Johnson A, Nehl C, Mason M. Hafner J. Fluid Electric Force Microscopy for Charge Density Mapping in Biological Systems. Langmuir. 19 [2001] 10007-100010.

4.14 Griesser H, Patrick G, Hartley S, McArthur K, McLean M. Interfacial Properties and Protein Resistance of Nano-Scale Polysaccharide Coatings; Smart Material Structure. 11 [2002] 652–266.

4.15 Ducker WA, Senden T, Pashley R. Direct measurement of colloidal forces using an atomic force microscope. Nature. 353, 6341 [1991] 239–241.

4.16 Martin Y, Abraham D, Wickramasinghe H. High-Resolution Capacitance

Measurement and Potentiometry by Force Microscopy. Appl Phys Lett. 52 [1998] 1103-1105.

4.17 Israelachvili JN. Intermolecular and Surface Forces, Second Edition. Academic Press. London. 1992.

4.18 Ide Y. Degradation of human hair proteins and of the protein films with the proteases. Kobunshi Ronbunshu. 61, 3 [2004] 190-193.

4.19 Parsegian VA Gingell D. On the electrostatic interaction across a salt solution between two bodies bearing unequal charges. J Biophys. 12 [1972] 1192-1204.

4.20 Nishiyama K, Kubo A, Ueda A, Taniguchi I. Surface pKa of Amine-Terminated Self-assembled Monolayers Evaluated by Direct Observation of Counter Anion by FT-Surface Enhanced Raman Spectroscopy. Chem Lett [2002] 80-81.

4.21 Kim J, David S, The Photostability of Shrinkproofing Polymer Systems on Wool Fabric; Polymer Degradation and Stability. 38 [1992] 131-37.

4.22 Bain CD, Troughton EB, Tao YT, Evall J, Whitesides GM, Nuzzo RG. Formation of Langmuir-Blodgett Films of a Fullerene. J Am Chem Soc. 111 [1989] 321-334.

4.23 Yukio N, Yamane S, Kida A. Adsorbable Organic Halides (AOX), AOX Formation Potential, and PCDDs/DFs in Landfill Leachate and their Removal in Water Treatment Processes; Journal of Material Cycles and Waste Management. 3 [2001] 126-134.

4.24 Rivett D. Structural lipids of the wool fiber. Wool Science Review. [1991] 1-25.

4.25 Dawson RCM, Elliott DC, Elliott WH, Jones KM, Data for Biochemical Research, Oxford, Clarendon Press, 1959.

4.26 Robinson GN, Kebabian PL, Freedman A, DePalma V. Temperature-dependent surface potentials of fluorinated alkanethiolate self-assembled monolayers. Thin Solid Films. 310, 1-2 [1997] 24-28.

REFERENCES

Appendix A

A.1 Chehroudi B, Gould TRL, Brunette DM. A light and electron microscopic study of the effects of surface topography on the behavior of cells attached to titanium-coated percutaneous implants. J Biomed Mater Res. 25, 3 [2004] 387-405.

A.2 Pramatarova L, Pecheva E, Krastev V, Riesz F. Ion implantation modified stainless steel as a substrate for hydroxyapatite deposition. Part I. Surface modification and characterization. J Mater Sci Mater Med. 18, 3 [2007] 435-40.

A.3 Gray D, Tien J, Chen C. Repositioning of cells by mechanotaxis on surfaces with micropatterned Young's modulus. J Biomed Mater Res A. 66 [2003] 605-14.

A.4 Lo CM, Wang HB, Dembo M, Wang YL. Cell movement is guided by the rigidity of the substrate. Biophys. J. 79, 144 [2000] 144-52.

A.5 Yeung T, Georges PC, Flanagan LA, Marg B, Ortiz M, Funaki M, Zahir N, Ming W, Weaver V, Janmey PA. Effects of Substrate Stiffness on Cell Morphology, Cytoskeletal Structure, and Adhesion. Cell Motility and the Cytoskeleton 60 [205] 24–34.

A.6 Bassiouni M, Bassiouni B. Proceedings of the 1st IEEE International Workshop on Intelligent Systems Techniques for Wireless Sensor Network, October [2006] 604–609.

A.7 Hu F, Kumar S, Xiao Y. Proceedings of the 4th IEEE Consumer

Communications and Networking Conference.

A.8 Jones, JR. Observing Cell Response to Biomaterials. Mater Today. 9, 12 [2006] 33-43.

A.9 Flemming RG, Murphy CJ, Abrams GA, Goodman SL, Nealey PF. Effects of synthetic micro- and nano-structured surfaces on cell behavior. Biomaterials. 20 [1999] 573– 88.

A.10 Rechnor JB, Recknor JC, Sakaguchi DS, Mallapragada SK. Oriented astroglial cell growth on micropatterned polystyrene substrates. Biomaterials. 25, 14 [2004] 2753–2767.

A.11 Recknor J, Sakaguchi DS, Mallapragada SK. Directed growth and selective differentiation of neural progenitor cells on micropatterned polymer substrates. Biomaterials. 27, 22 [2006] 4098-4108.

A.12 Dalton B, Walboomers XF, Dziegielewski M, Modulation of epithelial tissue and cell migration by microgrooves. Biomed Mater Res. 56 [2001] 195–207.

A.13 Jin CY, Zhu BS, Wang XF, Lu QH, Chen WT, Zhou XJ. Nanoscale surface topography enhances cell adhesion and gene expression of madine darby canine kidney cells. J Mater Sci Mater Med.19 [2008] 2215–2222.

A.14 Kinney J, Balooch M, Marshall S, Marshall G Jr, Weihs T. Atomic force microscope measurements of the hardness and elasticity of peritubular and intertubular human dentin. J Biomech Eng. 118, 1 [1996] 133-135.